Received: 16 March 2022 | Revised: 21 July 2022 | Accepted: 23 September 2022

DOI: 10.1002/jex2.65

RESEARCH ARTICLE

# Defective mitochondria-lysosomal axis enhances the release of extracellular vesicles containing mitochondrial DNA and proteins in Huntington's disease

**Margarida Beatriz**[1,2] | **Rita Vilaça**[1,2] | **Sandra I. Anjo**[1,3] | **Bruno Manadas**[1] | **Cristina Januário**[4] | **A. Cristina Rego**[1,4] | **Carla Lopes**[1,2]

[1]CNC-Center for Neuroscience and Cell Biology, CIBB - Centre for Innovative Biomedicine and Biotechnology, University of Coimbra, Coimbra, Portugal

[2]IIIUC-Institute for Interdisciplinary Research, University of Coimbra, Coimbra, Portugal

[3]Multidisciplinary Institute of Ageing, University of Coimbra, Coimbra, Portugal

[4]FMUC-Faculty of Medicine, University of Coimbra, Coimbra, Portugal

**Correspondence**
Carla Lopes, CNC-Center for Neuroscience and Cell Biology, University of Coimbra, Coimbra, Portugal.
Email: carla.lopes@cnc.uc.pt

Ana Cristina Carvalho Rego, Center for Neuroscience and Cell Biology, and Faculty of Medicine, University of Coimbra – polo I, Rua Larga, 3004–504 Coimbra, Portugal.
Email: acrego@cnc.uc.pt; arego@fmed.uc.pt

**Funding information**
This work was supported by the European Regional Development Fund (ERDF), through the Centro 2020 Regional Operational Programme under project CENTRO-01-0145-FEDER-000012-HealthyAging2020, and through the COMPETE2020–Operational Programme for Competitiveness and Internationalization and Portuguese national funds via FCT- Fundação para a Ciência e a Tecnologia, under project POCI-01-0145-FEDER-029621 and UIDB/04539/2020 and by Fundação Luso-Americana para o Desenvolvimento (FLAD) Life Science 2020 project.

## Abstract

Mitochondrial and autophagy dysfunction are mechanisms proposed to be involved in the pathogenesis of several neurodegenerative diseases. Huntington's disease (HD) is a progressive neurodegenerative disorder associated with mutant Huntingtin-induced abnormalities in neuronal mitochondrial dynamics and quality control. Former studies suggest that the removal of defective mitochondria may be compromised in HD. Mitochondrial quality control (MQC) is a complex, well-orchestrated pathway that can be compromised through mitophagy dysregulation or impairment in the mitochondria-lysosomal axis. Another mitochondrial stress response is the generation of mitochondrial-derived vesicles that fuse with the endolysosomal system and form multivesicular bodies that are extruded from cells as extracellular vesicles (EVs). In this work, we aimed to study the presence of mitochondrial components in human EVs and the relation to the dysfunction of both mitochondria and the autophagy pathway. We comprehensively characterized the mitochondrial and autophagy alterations in premanifest and manifest HD carriers and performed a proteomic and genomic EVs profile. We observed that manifest HD patients exhibit mitochondrial and autophagy impairment associated with enhanced EVs release. Furthermore, we detected mitochondrial DNA and proteins in EVs released by HD cells and in neuronal-derived EVs including VDAC-1 and alpha and beta subunits of ATP synthase F1. HD-extracellular vesicles transport higher levels of mitochondrial genetic material in manifest HD patients, suggesting an alternative pathway for the secretion of reactive mitochondrial components. This study provides a novel framework connecting EVs enhanced release of mitochondrial components to mitochondrial and lysosomal dysfunction in HD.

**KEYWORDS**
autophagy, extracellular vesicles, Huntington's disease, mitochondrial DNA, mitochondrial dysfunction, neuronal-derived extracellular vesicles

Margarida Beatriz and Rita Vilaça contributed equally to the present study.

# 1 | INTRODUCTION

Huntington's disease (HD) is an autosomal dominant neurodegenerative disease caused by an elongation of the CAG triplet in the exon 1 of the *huntingtin* gene (MacDonald et al., 1993). This pathology affects mainly the medium spiny neurons in the basal ganglia and to a lesser extent cortical areas that together drive motor coordination (Mehrabi et al., 2016; Vonsattel et al., 2008). Hence, involuntary movements are one of the symptoms, jointly with early manifestations including cognitive and emotional alterations (Beglinger et al., 2010; Lemiere et al., 2004; Thompson et al., 2012). Although the monogenic nature of the disease has been recognized for almost three decades, there is no cure or treatment to mitigate the progression. The study of biomarkers specific for different stages of HD is a step forward to monitor patients' conditions at the early stages of diagnosis and to adapt possible treatments. Until now the studies failed to show a consistently reproducible and clinically valid biomarker for HD, although numerous efforts are underway for the discovery of a reliable biomarker.

Mitochondrial dysfunction has been associated with neurodegenerative processes, including HD pathophysiology (reviewed in Carmo et al., 2018). In accordance, several mitochondrial parameters are altered in HD, including deficits in ATP production, increased reactive oxygen species (ROS) production, fragmented morphology, and reduced mitochondrial movement (Lopes et al., 2020; Shirendeb et al., 2012). In line with these results, other studies have described the negative impact of mutant huntingtin (mHTT) on mitophagy machinery, leading to the accumulation of dysfunctional mitochondria (Franco-Iborra et al., 2021). The mitochondrial protein quality control is tightly regulated by processes such as mitophagy, dynamics and stress responses that depend on mitochondrial chaperones and proteases. When those mechanisms fail to counteract mitochondrial damages, dysfunctional mitochondria cause enhanced oxidative stress, bioenergetic deficits and neurodegeneration (Jędrak et al., 2018; Lopes et al., 2022).

Extracellular vesicles (EVs) are nanosized particles that act as intercellular communicators and can be defined according to size in small EVs (< 200 nm) and large EVs (> 200 nm) (Théry et al., 2018). EVs are secreted by all cell types, including neurons, microglia and fibroblasts to transport cell-specific molecules like proteins, lipids, RNA, and DNA fragments from donor cells that can alter gene expression and function of recipient cells (O'Brien et al., 2020). The study of EVs dynamics has expanded exponentially over the past few years, particularly in neurodegenerative diseases. EVs are believed to play a role in the development and progression of neurodegenerative diseases by carrying disease-associated miRNAs and/or proteins and therefore EVs cargo may provide important biomarkers for diagnosis (reviewed in Beatriz et al., 2021).

Recent work has revealed an intimate interconnection between classical autophagy machinery and autophagy-dependent EVs pathways that facilitates the disposal of unwanted genetic material and proteins (Leidal et al., 2020). Additionally, recent evidence suggests that EVs transfer mitochondrial DNA (mtDNA) and mitochondrial proteins intercellularly (Sansone et al., 2017; Todkar et al., 2021; Wang et al., 2020); however, the biological relevance, the mechanisms underlying this process and the contribution in pathophysiological contexts are not clear.

Neuronal-derived EVs (NDE) are a subpopulation of the central nervous system (CNS)-derived EVs that can be isolated from human fluids, including blood plasma and cerebrospinal fluid, to investigate their neuron-specific contents (Yousif et al., 2021). The presence of specific neuronal biomarkers in NDE isolated from blood samples of patients with amyotrophic lateral sclerosis (ALS), Alzheimer or Parkinson's disease, recognizing their potential to monitor disease status and progression (Jia et al., 2020; Katsu et al., 2019; Niu et al., 2020).

With the objective of studying the crosstalk between the release of EVs and malfunction of mitochondrial discard processes, in this work we characterized mitochondrial function and autophagy/mitophagy dynamics in cells from HD carriers and controls (CTRs) individuals. Additionally, we isolated EVs secreted by these cells and NDE from the same patients' biofluids and analysed proteomic and genomic content. Our findings suggest that mitochondrial dysfunction associated with impaired autophagy enhances EVs release and this mechanism could act as an alternative pathway for the secretion of mitochondrial cargo in HD.

# 2 | MATERIALS AND METHODS

## 2.1 | Cell culture and reagents

Human dermal fibroblasts were obtained from skin explants of HD carriers and CTRs, as described previously (Lopes et al., 2022). The 'manifest' and 'premanifest' terms were applied to HD carriers with and without onset of motor alterations, respectively. Fibroblasts were cultured in DMEM medium (Gibco), supplemented with 9 mM sodium bicarbonate, 10% foetal bovine serum (FBS) (Gibco) and 1% penicillin/streptomycin (Gibco). Cells were maintained in an incubator at 37°C with 5% $CO_2$ for no more than 15 passages. The assays were performed in three premanifest (fpHD1, fpHD2, fpHD3) and two manifest HD fibroblasts lines (fHD1 and fHD2) versus control lines (fCTR1, fCTR2, fCTR3).

Dermal fibroblasts were successfully reprogrammed into induced-pluripotent stem cells (iPSC) using non-integrating Sendai virus for transduction, as described previously (Schlaeger et al., 2015). iPSC were grown and maintained in Geltrex with StemFlex

medium (Gibco) and the generation and proliferation of neural stem cells (NSC) was done as previously (Lopes et al., 2020). Briefly, to differentiate NSC toward a striatal-specific neuronal phenotype, until day 5 of differentiation, neuronal induction media was supplemented with 5 $\mu$M Dorsomorphin (Sigma) and 10 $\mu$M SB431542 (Peprotech) and later added 1 $\mu$M XAV 939 (Peprotech) and 200 ng/ml sonic hedgehog (SHH C-25II) (R&D) until day 12 (Chambers et al., 2009; Delli Carri et al., 2013; Nicoleau et al., 2013). At that point, NSC were dissociated with accutase (GRiSP), and plated on Geltrex-coated coverslips in 24-well plates. To further obtain mature striatal-like neurons, from day 15 to 25 N2/B27 medium was supplemented with 200 ng/ml SHH, 1 $\mu$M XAV939 and 30 ng/ml brain-derived neurotrophic factor (BDNF) (Peprotech). From day 26 onward only 50 ng/ml BDNF was added to the medium and medium changed every 3 days (Figure S1a). The two HD-NSC lines, nHD1 and nHD2, were obtained from iPSC reprogrammed of fibroblasts lines fHD3 and fHD1, respectively, and the two CTR-NSC lines, nCTR1 and nCTR2, were obtained from iPSC reprogrammed of fibroblasts lines fCTR3 and fCTR1, respectively.

## 2.2 | Construction of plasmids and viral production

The lentivirus pLESIP-GFP-LC3 was a kind gift from Dr. Ola Awad (University of Maryland, USA). pCL6EGwo and pCL6-CD63eGFP were a kind gift from Dr. Helmut Hanenberg and Dr. Bernd Giebel (University of Duisburg-Essen, Germany). The 86 bp insert of Mito-DsRed2 (Clontech) was subcloned at the NheI and BsrGI sites of the pCL6EGwo vector using standard recombinant DNA technology (pCL6-Mito-DsRed2). The pCL6-CD63eDsRed was constructed by cloning the 709 bp CD63 insert into the previous plasmid using NheI and *Bam*HI restriction. For the preparation of high-titre lentiviral stock lentiviral particles were produced in HEK293T cells by transiently co-transfecting the described plasmids with psPAX2 (#12260, Addgene) and pCMV-VSV-G (#8454, Addgene) using JetPrime reagent (Polyplus-transfection). After 48 h, the viral particles were collected from the medium, purified and concentrated as described previously (Tiscornia et al., 2006). Lentiviral titration was estimated on FACS based on fluorescence.

## 2.3 | Incubation of fibroblasts with chloroquine and FCCP

With the objective of evaluating autophagic flux by western blotting, fibroblasts were incubated with 60 $\mu$M chloroquine (CQ) (Sigma) and 10 $\mu$M FCCP (CSNpharma) for 16 h in EVs-depleted medium, using DMSO as control. EVs were isolated from the same cell culture media, as described. The number of EVs was assessed by Nanosight Tracking Analysis (NTA), and DNA was extracted to evaluate the mitochondrial DNA copies. As a control for EVs release, cells were incubated with 30 $\mu$M of GW4869 (CSNpharma) for 24 h. For immunocytochemistry experiments, MitoDsRed and pLESIP-GFP-LC3 transduced cells were incubated with 100 $\mu$M CQ and 30 $\mu$M FCCP for 5 h.

## 2.4 | Live cell microscopy

Fibroblasts were transduced either with pCL6-CD63eDsRed or pCL6-CD63eGFP vectors. Upon CD63+ expression, a 1:1 ratio was seeded for 24 h in IBIDI $\mu$-Dish, 35 mm high (IBIDI, Germany). Rapid time-lapse imaging was performed using a Zeiss Cell Observer Spinning Disk System (Carl Zeiss Microscopy) (Plan-Apochromat 63x/1.4 Oil DIC objective) with an incubation system creating a 37°C environment. Cells were imaged for up to 6 min. Particle tracking and trajectory analysis were performed with the Imaris x64 software version 9.5. Single-particle tracking trajectories are shown as dragon tail visualization. Speeds were derived from relative EVs displacement between two frames. The spots were quantified with a minimum xy diameter of 0.3 $\mu$m, a max distance of 100 $\mu$m, the quality threshold of 600–3000 and a track duration of 1,5 s. The parameters analysed were: Track length- total length of trajectory; Track straightness- relative measure for track straightness with 0 representing random diffusion and 1 representing a straight line.

## 2.5 | Cellular oxygen consumption and extracellular acidification rates

The oxidative phosphorylation and glycolytic levels of NSC were assessed through the measurement of the oxygen consumption rate (OCR) and extracellular acidification ratio (ECAR), respectively, on a Seahorse XFe96 apparatus (Agilent) as previously described (Lopes et al., 2020). One day before the experiments, NSC were seeded in a Geltrex-coated XF96 Cell Culture Microplate at a density of 15,000 cells per well. For measuring the OCR, the apparatus added to cells, in the following order, 1 $\mu$M oligomycin (Alfa Aesar), 1 $\mu$M FCCP and 1 $\mu$M rotenone (Sigma) plus 1 $\mu$M antimycin (Sigma). For measuring the ECAR, the apparatus added to the cell media, in the following order, 10 mM glucose (Sigma), 1 $\mu$M oligomycin (Alfa Aesar) and 50 mM

2-deoxyglucose (DOG) (Sigma). The final measurements were normalized to protein content using sulforhodamine B (Sigma) (Johnson et al., 2016).

## 2.6 | Transfection

NSC and neurons were transfected with Lipofectamine 3000 Transfection Reagent (Invitrogen) according to the manufacturer's protocol. Briefly, cells were plated in 24-well plates and transfected with 1.5 $\mu$g/$\mu$l psDsRed-2Mito plasmid (Clontech).

## 2.7 | Mitochondrial movement

At day 80 of differentiation, transfected (psDsRed-2Mito) striatal-like neurons were washed with Hanks' Balanced Salt solution (HBSS) (#14025, Thermo Fisher Scientific). Mitochondrial movement videos were acquired on a Zeiss Cell Observer Spinning Disk System (Carl Zeiss Microscopy). For reference purposes, a static image of the neuron was acquired, and mitochondrial movement was recorded for 3 min with a 300 ms interval. Using the *TurboReg* plug on ImageJ, the video fluctuation was corrected. The *KymoToolBox* assembly of plugs produced a kymograph for each video, representing the mitochondrial movement across the timeline. Analyzed Kymo presented a set of parameters: velocity, persistence (Persistence = total distance travelled/distance in a straight line between the initial and final point; reflects the distance travelled in the same direction) distance travelled and time spent moving (anterograde- from the axon terminal to the soma- and retrograde- from the soma to the axon terminal movement) (Zala et al., 2013).

## 2.8 | Immunocytochemistry and image processing

Cells were washed with pre-warmed PBS at 37°C, permeabilized with PHEM/0.1% Triton and fixed with PHEM/4% Paraformaldehyde (PFA) for 20 min. Blocking was performed for 40 min using PHEM/0.1% Triton/3% bovine serum albumin (BSA). The following primary antibodies were used: anti-P62 (SQSTM1) (1:100, #814802, BioLegend), anti-CD107b (LAMP-2) (1:100, #354301, BioLegend), anti-PINK1 (1:100, #846201, BioLegend), anti-LC3A/B (1:400, #12741S, Cell Signalling Technology), anti-OPA1 (1:50, #612606, BD Biosciences), anti-MFN2 (1:500, #M6319, Sigma), anti-DRP1 (1:100, #ab56788, Abcam), anti-nestin (1:200; #MAB1259 R&D), anti-DARPP32 (1:500, #40801, Abcam), anti-synaptophysin (1:500, #ab32127, Abcam). After, cells were incubated with secondary antibodies for 1 h at room temperature (RT) and mounted using Mowiol (Sigma); Hoechst (Invitrogen) was used to stain the nuclei. Images were acquired on a Zeiss LSM 710 Confocal System (Carl Zeiss Microscopy). Analysis of mitochondrial morphology was performed using Fiji ImageJ software. The area of the cell was established by drawing a ROI in the psDsRed-2Mito channel. The following mitochondrial parameters were obtained: number and area normalized to cell area; aspect ratio, which represents the elliptic shape of mitochondria; Feret's diameter, which represents the distance between the two more far apart points of the mitochondria, reflecting the complexity of these organelles' structure; Form factor that represents the branching of the mitochondrial net; and Circularity which describes more mature and elongated mitochondria for the value of 0 and circular and, so, more immature mitochondria for the value of 1 (Merrill et al., 2017). The equations that describe some of these parameters follow below:

- $$\text{Aspect ratio} = \frac{\text{major axis}}{\text{minor axis}}$$

- $$\text{Form factor} = \frac{\text{perimeter}^2}{4\pi \times \text{area}}$$

- $$\text{Circularity} = \frac{4\pi \times \text{area}}{\text{perimeter}^2}$$

Colocalization studies of fusion/fission proteins with mitochondria were performed on Z-stacks using the JACoP ImageJ plugin.

## 2.9 | Western blotting

Cells were lysed in a lysis buffer supplemented with 1:1000 protease inhibitor cocktail (Sigma), and protein was quantified using the Bio-Rad Protein Assay (Bio-Rad). For protein denaturation, SDS sample buffer was added to protein lysates (30 $\mu$g for fibroblasts, 25 $\mu$g for NSC) for 5 min at 95°C. Samples were then loaded into 6%–15% acrylamide gels. For EVs, the final isolated pellet (from 150 ml of fibroblasts or 60 ml of NSC culture media) was lysed in RIPA buffer and then protein was denatured in SDS sample buffer (non-reducing conditions were used to assess CD63 presence). Samples were then loaded into 10%–12% acrylamide gels. Samples were resolved in an SDS-PAGE and transferred onto methanol-activated polyvinylidene difluoride (PVDF) Hybond-P membranes. Membranes were blocked in TBS-T/5% BSA for 1 h at RT and incubated overnight at 4°C with anti-P62 (SQSTM1) (1:500, #814802, BioLegend), anti-CD107b (LAMP-2) (1:250, #354301, BioLegend), anti-PINK1 (1:1000, #AP6406B, Abcepta), anti-LC3A/B (1:250) (#12741S, Cell Signaling), anti-$\beta$-Actin (1:5000, #D6A8, Cell Signaling) anti-$\beta$-Actin (1:5000, Sigma, #A5316), anti-OPA1 (1:500, #612606, BD Biosciences), anti-MFN2 (1:1000, #M6319, Sigma), anti-p-DRP (1:1000, #3455S, Cell Signalling), anti-DRP1 (1:1000, #ab56788, Abcam), anti-FIS1 (TTC11) (1:1000, #NB100-56646, Novus), anti-Alix (1:100, #sc-53538, Santa Cruz), anti-flotillin-2 (C42A3) (1:500, #3436,Cell Signalling), anti-calnexin (1:500) (#ab10286, Abcam) and anti-CD63 (TS63) (1:500, #10628D, Life Technologies). Primary antibodies were washed with TBS-T and membranes were incubated with secondary antibodies anti-mouse and anti-rabbit (1:5000) diluted in TBS-T/1% BSA for 1 h at RT. Secondary antibodies were washed and immunoreactive bands were developed for 5 min with ECF (GE Healthcare) and revealed in a Chemidoc Imaging System (Bio-Rad) (in Lopes et al., 2020).

## 2.10 | Dot blotting

Samples were loaded directly onto methanol-activated PVDF membranes and left to dry at RT. Membranes were blocked in TBS-T/5% BSA for 1 h at RT and incubated overnight at 4°C with anti-CD63 (TS63) (1:500, #10628D, Life Technologies), anti-CD171 (L1CAM) (1:200, #13-1719-82, Thermo Fisher) and anti-synaptophysin (YE269) (1:500, #ab32127, Abcam). The following procedure was similar to western blotting.

## 2.11 | EVs and NDE isolation and characterization

For small EVs isolation (< 200 nm), fibroblasts were cultured in EVs-depleted medium, by centrifuging FBS previously at 100,000 ×*g* for 18 h at 4°C to pellet animal vesicles. The term "EVs" was further applied to refer to the vesicles (< 200 nm) isolated in this study. For isolation of EVs of fibroblasts and NSC, cell culture supernatant was collected every other day and stored at -80°C for posterior use. For isolation of sEVs in bulk, culture media was thawed at 37°C and filtered (0.22 $\mu$m) to remove cell debris and proceed as described (Théry et al., 2006). Briefly, medium was centrifuged at 10,000 ×*g* for 30 min, and twice at 100,000 ×*g* for 70 min to pellet EVs. EVs were resuspended in different buffers depending on the final use: PBS for DNA extraction, NTA and mass spectrometry; PBS/2% PAF for transmission electron microscopy (TEM) and RIPA for western/dot blotting.

## 2.12 | Isolation of EVs from blood plasma

Blood samples were obtained from HD carriers and healthy CTRs upon informed consent. Blood was collected into collection tubes with K2EDTA (BD Vacutainer Plastic Blood Collection Tubes). Plasma was the preferred source of EVs because serum contains additional EVs that are released from platelets during *in vitro* clot formation (Coumans et al., 2017). Briefly, blood was diluted 1:1 in PBS and isolated by a Ficoll (GE Healthcare, Fisher Scientific) density gradient separation performed at 800 *xg* for 30 min at RT, no break. Plasma was kept at -80°C until further use.

EVs from blood plasma were isolated using the exoEasy Maxi kit (Qiagen) following the manufacturer's protocol. The pellet was resuspended in 300 $\mu$l of Resuspension Buffer. The total plasma EVs were stored at −80°C until required for NTA and dot blot analysis and further isolation of NDE.

## 2.13 | Neuronal-enriched EV extraction

NDE were isolated from total EVs of plasma using the Basic Exo-Flow Capture Kit (System Biosciences) as described (Winston et al., 2019). First, 40 $\mu$l of streptavidin magnetic beads were incubated with 4 $\mu$g of anti-CD171 (L1CAM, neural adhesion protein) biotinylated antibody (clone 5G3, #13-1719-82, Thermo Fisher) for 3 h on ice. After, the beads were suspended in Bead Wash Buffer

and 100 $\mu$l of total EVs previously isolated from plasma was added. To allow the magnetic beads to capture the desired vesicles, the complexes were left overnight gently rotating at 4°C. The beads were washed and EVs/NDE were eluted in exosome elution buffer and stored at -80°C until further required.

## 2.14 | Particle size and concentration analysis

EVs were resuspended in 1 ml of water containing low-mineral concentration. NTA analysis was performed in a NanoSight NS300 instrument with a sCMOS camera module (Malvern Panalytical), following general recommendations. Analysis settings were optimized and kept constant between samples. The videos were analysed to obtain the mean size and estimated concentration of particles. Data were processed using the NTA 3.1 analytical software.

## 2.15 | TEM and immunogold-TEM

EVs were isolated from culture media of fibroblasts and NSC. The antibody anti-TFAM (1:150, #sc-28200, Santa Cruz) were used for immunoelectron labelling. Briefly, samples were placed on carbon-Formvar coated 300 mesh nickel grids, and samples were allowed to absorb for 20 min. Following washing in PBS (2 × 3 min), grids were floated (sample side down) onto 50 $\mu$l drops of 50 mM glycine (4 × 3 min) to quench free aldehyde groups and then transferred to blocking solution (5% BSA, 0.01% saponin in PBS) for 10 min. Then, grids were incubated in blocking buffer (1% BSA, 0.01% saponin in PBS; negative control) or primary antibodies for 2 h followed by washing steps in BSA 1% (6 × 3 min). Secondary antibodies (anti-rabbit IgC immunogold conjugates, 1:200) were then added for 1 h, followed by additional washing steps (8 × 2 min). After, samples were fixed in glutaraldehyde 1% for 5 min and washed in water (8 × 2 min). A final contrasting step was performed using uranyl-oxalate solution pH 7, for 5 min followed by a mixture of 4% uranyl acetate and 2% methyl cellulose for 10 min on ice. Imaging was conducted using a FEI-Tecnai G2 Spirit Bio Twin TEM at 100 kV.

## 2.16 | SWATH-MS analysis

The pellets of EVs were dissolved in 2x SDS-PAGE Sample Loading Buffer (Nzytech) aided by ultrasonication. Each sample was spiked with the same amount of a recombinant protein (MBP-GFP) to be used as internal standard (Anjo et al., 2019) and denatured at 95°C for 5 min. A small part of each denatured sample was pooled to generate the proteome library (protein composition of each condition), and the remaining sample was used separately for SWATH-MS analysis to extract quantitative information. Samples were then alkylated with acrylamide and subjected to in-gel digestion by using the short-GeLC approach (Anjo et al., 2015).

All samples were analysed on a NanoLC™ 425 System coupled to a Triple TOF™ 5600 mass spectrometer (Sciex) using two acquisition modes: (i) the pooled samples were analysed by information-dependent acquisition (IDA) and, (ii) the individual samples by SWATH-MS mode. The ionization source was the DuoSpray™ Ion Source (Sciex) with a 50 $\mu$m internal diameter (ID) stainless steel emitter (NewObjective).

For IDA experiments, the mass spectrometer was set to scanning full spectra (m/z 350–1250) for 250 ms, followed by up to 100 MS/MS scans ($m/z$ 100–1500) per cycle, in order to maintain a cycle time of 3.309s. The accumulation time of each MS/MS scan was adjusted in accordance with the precursor intensity (minimum of 30 ms for precursor above the intensity threshold of 1000). Candidate ions with a charge state between +2 and +5 and counts above a minimum threshold of 10 counts per second were isolated for fragmentation and one MS/MS spectrum was collected before adding those ions to the exclusion list for 25 s (mass spectrometer operated by Analyst TF 1.7, Sciex). The rolling collision was used with a collision energy spread (CES) of 5. For SWATH experiments, the mass spectrometer was operated in a looped production mode (Gillet et al., 2012) and specifically tuned to a set of 60 overlapping windows, covering the precursor mass range of 350–1250 m/z. A 200 ms survey scan (350–1250 m/z) was acquired at the beginning of each cycle, and SWATH-MS/MS spectra were collected from 100 to 1500 m/z for 50 ms resulting in a cycle time of 3.254 s. The collision energy for each window was determined according to the calculation for a charge +2 ion centred upon the window with variable CES, according to the window.

Peptide identification and library generation were performed by searching all the IDA samples using the ProteinPilot™ software (v5.1, ABSciex) with the following parameters: (i) search against a database from SwissProt composed by Homo Sapiens (release in March 2019) and MBP-GFP (IS) sequences; (ii) acrylamide alkylated cysteines as fixed modification; and (iii) trypsin as digestion type. An independent False Discovery Rate (FDR) analysis using the target-decoy approach provided with Protein Pilot software was used to assess the quality of the identifications and positive identifications were considered when identified proteins and peptides reached a 5% local FDR (Sennels et al., 2009; Tang et al., 2008). Complementary/Further information can be found in Supplementary material.

## 2.17 | Systematic analysis

Biological and molecular processes terms from Gene Ontology were analyzed using PANTHER (http://www.pantherdb.org/). The protein–protein interaction network and identification count were obtained from the STRING database (http://string-db.org/) and the EVpedia database (https://evpedia.info), respectively.

## 2.18 | DNA/RNA extraction, cDNA and PCR

Genomic DNA was extracted using PureLink Genomic DNA Kit and RNA with the PureZOL RNA Isolation Reagent according to the manufacturer's instructions. Reverse transcription was performed with iScript™ cDNA Synthesis Kit. Real-time PCR (qPCR) was performed with iQTM SYBR Green Supermix on a CFX96 Touch™ Real-Time PCR Detection System as previously described (Lopes, 2020). QPCR was performed according to the manufacturer's protocol. 18S was used as internal reference gene. Expression values were calculated using the $2^{-\Delta\Delta Ct}$ method. All PCR samples were run in technical triplicates, and the average Ct-values were used for calculations. CAG repeats number in cells was determined by PCR, as described previously (Evers et al., 2015). Primers used are listed in Table S1.

## 2.19 | Analysis of mitochondrial DNA copy number

EVs were isolated from FBS Exo-depleted culture media of fibroblasts and NSC and NDEs were extracted from blood plasma. To eliminate contaminant DNA, EVs resuspended in PBS, were pretreated with 10 $\mu$g/$\mu$l of DNAse I (Canvax), according to the manufacturer's instructions. EVs DNA (exoDNA) and cellular DNA were extracted with QIAamp DNA Micro Kit (QIAGEN) and DNeasy tissue and blood kit (QIAGEN), respectively, and DNA was eluted in 20 $\mu$l DEPC-treated water. The concentration and purity of DNA derived from EVs was assessed by measurement of absorbance and 260/280 ratio with a NanoDrop 2000/c (Thermo Fisher Scientific).

To detect the presence of mtDNA in EVs and cells, exoDNA (8 ng) or cell's DNA (6 ng) was used for whole mtDNA amplification according to (Dames et al., 2015). Briefly, long-range PCR was used to amplify the whole mtDNA sequence using three overlapping primer pairs. Each amplification was performed using Phusion High-Fidelity DNA polymerase (Thermo Scientific) and the amplicons were separated on a 0,8% agarose gel and visualized with a GelDoc system (Bio-Rad). Primers used are listed in Table S1.

## 2.20 | Quantification of mtDNA copies number

Quantification of absolute mtDNA copy number was performed as described in (Gonzalez-Hunt et al., 2016), with minor modifications. The method is based on real-time PCR assay using a standard curve with amplifying serial dilutions of a mtDNA-specific gene. The average Ct value of each DNA sample was used to interpolate with the standard curve to calculate the absolute number of copies of mtDNA gene. The standard curve was generated by cloning a short 100-bp sequence of mitochondrial 16S rRNA gene into pGEM-T Easy Vector (Promega). The 16S_rRNA gene sequence was amplified with Taq Polymerase (Supreme NZYtech II master mix) and cloned into pGEM-T easy vector. Briefly, 2 ng of ExoDNA was used to calculate mtDNA copies number with iQ SYBR Green Supermix (Bio-Rad) on a CFX96 Touch Real-Time PCR Detection System (Bio-Rad). Logarithmic regression was used to plot Ct values against a known number of copies and absolute mtDNA copies number for each sample was calculated as previously described (Gonzalez-Hunt et al., 2016). Primers used are listed in Table S1.

## 2.21 | Measurement of mitochondrial hydrogen peroxide production

Cells were plated in Geltrex-coated 96-well plates at a density of 15 000 cells per well the day before the experiments. To study mitochondrial ROS, cell media was removed, cells were washed with warm HBSS and incubated with 10 $\mu$M MitoPY1 (Sigma) for 20 min at 37 °C. Cells were washed twice with HBSS and MitoPY1 fluorescence (excitation- 503 nm, emission - 530 nm) was measured using a Fluorimeter SpectraMax GEMINI EM (Molecular Devices) or a Microplate Reader SpectraMax iD3 (Molecular Devices). Hydrogen peroxide basal production was measured for 10 min and for 30 min after the addition of 3 $\mu$M myxothiazol or 1 $\mu$M rotenone. Results obtained reflect RFUs from myxothiazol/rotenone stimulus normalized to RFUs from control wells (Lopes, 2022).

### 2.22 | Statistical analysis

Statistical computations were performed using GraphPad Prism version 9.0, GraphPad Software, La Jolla, CA, USA, and SPSS version 21.0 (IBM SPSS Statistics for Windows, IBM Corp). Statistical analysis was performed for individual subjects and among groups (CTRs, premanifest HD carriers and manifest HD patients). Results are the mean ± SEM of the indicated number of independent experiments in figures legends. For cell experiments, at least three independent assays were performed for each experimental condition. Statistical significance was analysed using parametric test, one-way ANOVA, followed by Bonferroni post hoc test and non-parametric test Kruskal Wallis followed by Dunn's multiple comparison test. Correlations were done using the Spearman rank correlation coefficient ($\rho$). $p < 0.05$ was considered significant.

## 3 | RESULTS

### 3.1 | Mitochondrial function and dynamics in differentiated neuronal cells

We have previously demonstrated that human NSC from HD patients exhibit features of mitochondrial and metabolic dysfunction (Lopes et al., 2020). iPSC reprogrammed from patients' fibroblasts (Lopes et al., 2022) were differentiated into progenitors and fully mature GABAergic striatal-like neurons, respectively, using published protocols (Figure S1a) (Delli Carri et al., 2013; Lopes et al., 2020). The CAG repeat expansion was confirmed in HD cell lines by PCR (Figure 1a). The successful differentiation of the iPSC into NSC was confirmed by the progenitor cell marker nestin and the expression of the specific marker DARPP32, at differentiation day 80, confirmed the maturation into striatal medium spiny neurons (Figure 1b).

First, we analysed mitochondrial bioenergetics and dynamic events in neuronal progenitors. HD-NSC exhibited reduced levels of basal respiration compared to CTRs, nHD1 NSC presented decreased maximal respiration compared to nCTR2, and lower spare respiratory capacity in nHD2 NSC relatively to nCTR2 cell line (Figure 1c, S1b). In addition, nHD2 NSC presented a reduction of glycolysis and glycolytic capacity compared to nCTR2 cell line (Figure 1d, Figure S1c). Together, these data suggest that HD neural progenitors have a decreased bioenergetic profile. Despite the metabolic alterations found in HD-NSC we did not find alterations in mitochondrial hydrogen peroxide production (Figure S1d, e).

The number of mtDNA copies has a crucial role in mitochondrial biogenesis and bioenergetics, which is regulated by the nuclear transcriptional factors PGC-1$\alpha$ (peroxisome proliferator-activated receptor gamma co-activator) and TFAM (mitochondrial transcription factor A). In accordance, analysis of the mRNA transcripts showed a tendency for decrease levels of PGC-1$\alpha$ in HD lines, although not significant, and lower levels of TFAM in HD-NSC, particularly for nHD1 compared to nCTR2. (Figure 1e). The quantification of mtDNA copies also showed a trend for lower values in these cells despite no statistical significance (nCTR2 vs. nHD2; $p = 0.0571$) (Figure 1e).

Since mitochondria are organelles that depend highly on dynamic mechanisms to maintain quality control, we sought to evaluate mitochondrial fission/fusion processes. The total levels of fission proteins (phospho-Drp, Drp1 and FIS1) and fusion proteins (Mitofusin2 and OPA1) were unaltered between HD-NSC and CTRs, although Mitofusin2 colocalize less with mitochondria in nHD1 versus nCTR1 cells and for DRP1 the colocalization was lower in nHD2 versus nCTR2 (Figure S2a, b). Mitochondrial morphological changes were further investigated in NSC transduced with pDsRed2Mito vector. HD-NSC had an overall higher mitochondria content and a decrease in Feret's diameter (greatest distance between two points). The other mitochondrial shape descriptors were indistinguishable between mitochondrial subpopulations (Figure 1f). To gain further insight into mitochondrial dynamics, mitochondrial movement was evaluated in differentiated post-mitotic striatal-like neurons in which mitochondria are more mature than in proliferative NSC (Beckervordersandforth et al., 2017). We observed slower mitochondrial velocity and reduced organelle distance travelled in HD striatal-neurites, associated with higher persistence meaning that mitochondria changed fewer times the direction of movement (Figure 1g).

### 3.2 | Auto(mito)phagy analysis in human fibroblasts

Our previous work described altered mitochondrial function and redox deregulation in fibroblasts from manifest HD patients (Lopes et al., 2022). Since dysfunctional/damaged mitochondria are removed through selective autophagy, more precisely mitophagy, we further analysed the levels of proteins involved in this process in three premanifest HD (fpHD) and two manifest HD (fHD) lines of fibroblasts (vs two fCTRs) to infer autophagy at different stages of the disease (Figure 2). Since defects in autophagic flux have been linked to HD (Pircs et al., 2018), we monitored autophagic activity by evaluating the levels of LC3-I, LC3-II/I ratio, p62 (proteins related to autophagosomal assembly and selective autophagy), LAMP2 (lysosomal constitution) and PINK1 (mitophagy ubiquitin-dependent pathway) by western blotting and immunocytochemistry. We found increased protein levels of the autophagic markers p62 in fpHD and fHD and LC3-I in fpHD, as well as the mitophagy marker PINK1 in fpHD and

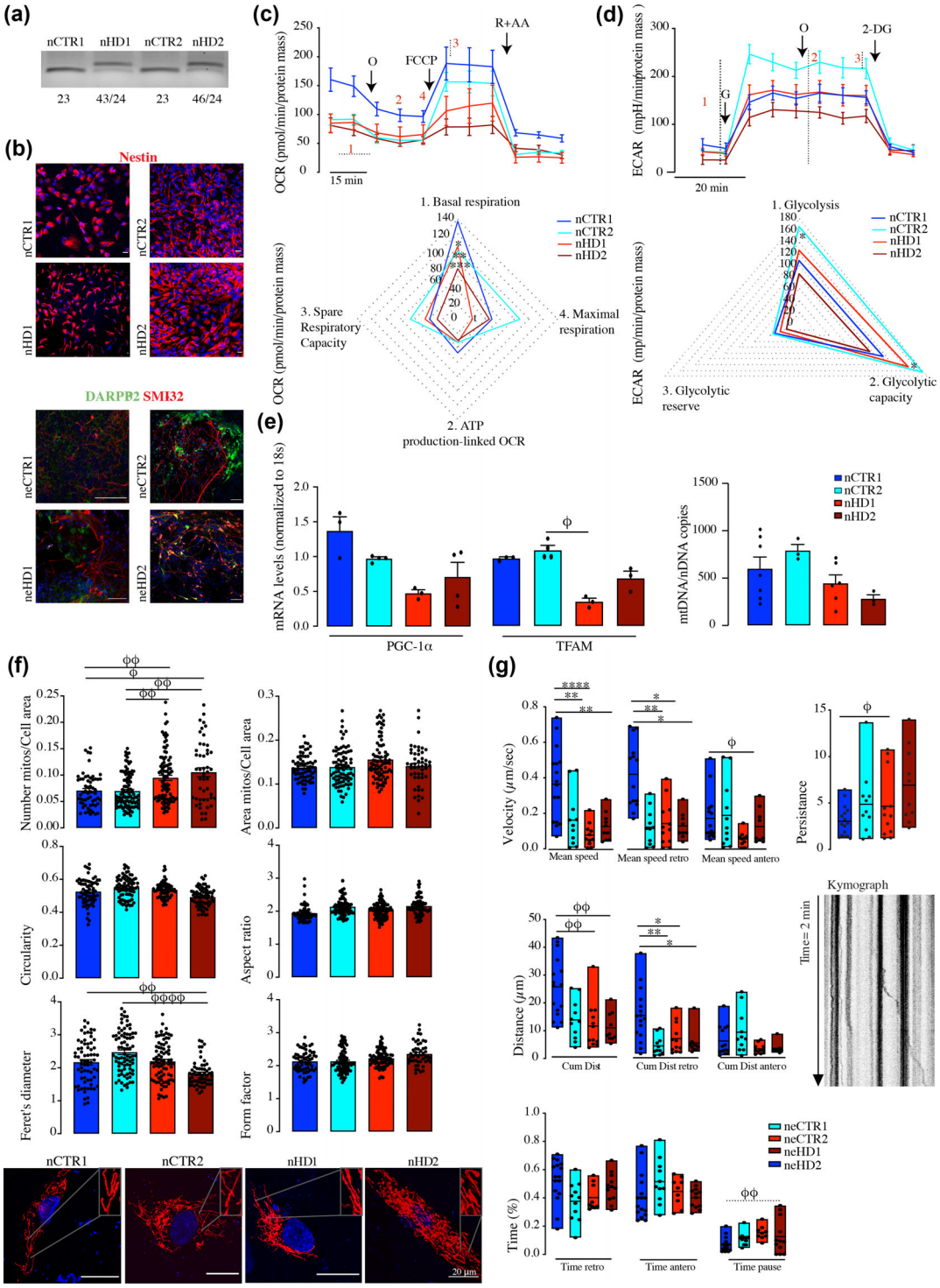


**FIGURE 1** Mitochondrial bioenergetic and dynamic abnormalities in HD and control differentiated NSC and striatal-like neurons. (a) PCR analysis of the CAG repeat expansion. (b) Expression of neural progenitors' marker Nestin at day 15 and SMI-32 positive medium spiny neurons at day 80 expressing striatal marker DARPP32 (scale bar = 50 $\mu$m). (c) Cellular oxygen consumption rate (OCR) graph shown on top and spider plots on the bottom: (1) basal respiration; (2) oxygen consumed for ATP generation; (3) Spare respiratory capacity; (4) maximal respiration capacity; (d) and extracellular acidification rate (ECAR) graph shown on top and spider plots on the bottom: (1) glycolysis; (2) glycolytic capacity, (3) glycolytic reserve in NSC from HD patients and controls ($N = 5$–10). Values for mean ± S.E.M of at least three independent experiments. (e) mRNA levels of PGC-1$\alpha$ and TFAM normalized to 18S, and mitochondrial DNA (mtDNA) copy number ($N = 3$–6). (f) Mitochondrial morphology, size and number in HD NSC versus CTR and representative images of mitochondria fluorescence after transfection with psDsRed-2Mito (scale bar = 20 $\mu$m) ($N = 48$–79). (g) Analysis of mitochondrial motion in striatal-like neurons transfected with psDsRed-2Mito and representative kymograph ($N = 10$–15). Bar plots represent mean ± S.E.M and floating bars show the minimum and maximum (line at mean). Statistical analysis: one-way ANOVA followed by Bonferroni post-hoc: * $p < 0.05$, ** $p < 0.01$, *** $p < 0.001$, **** $p < 0.0001$ or Kruskal-Wallis comparisons: $^{\varphi} p < 0.05$, $^{\varphi\varphi} p < 0.01$, $^{\varphi\varphi\varphi\varphi} p < 0.0001$

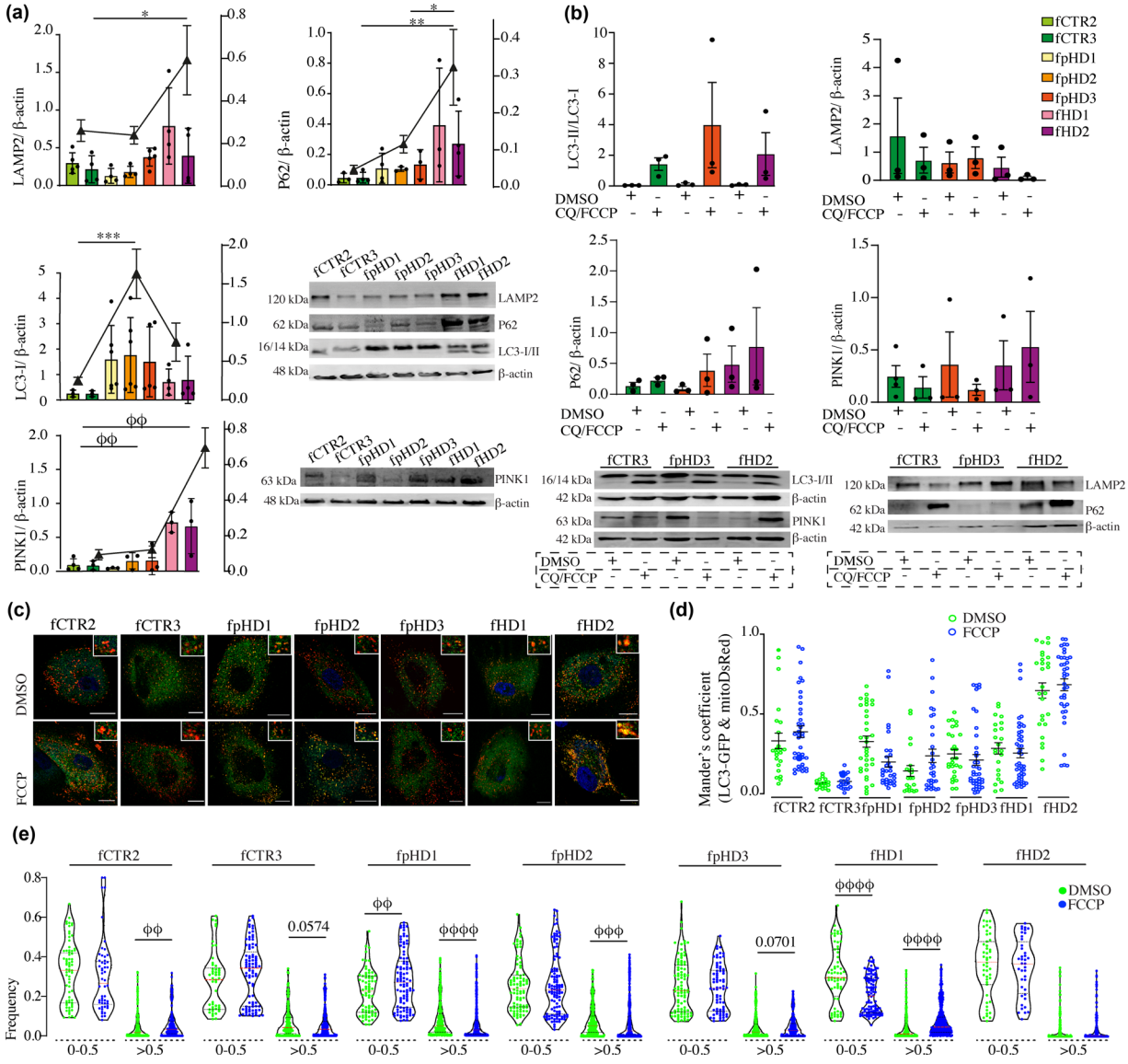


**FIGURE 2** Basal and dynamic autophagic flux in fibroblasts from HD patients and controls. (a) Western blot analysis of autophagy-associated protein markers LAMP2, p62, LC3-I and PINK1 in fibroblasts from HD patients and controls (two control, three premanifest and two manifest HD). Fibroblasts were grouped for purposes of comparison as presented in the right YY axis. Results were normalized to ß-actin levels ($N = 4$). (b) Analysis of autophagic flux by western blotting in one cell line per group treated with chloroquine (CQ) (60 $\mu$M) and FCCP (10 $\mu$M) for 24 h to block lysosomal acidification and promote mitophagy. Results were normalized to ß-actin levels ($N = 3$). Colocalization represented by (d) Mander's coefficient, of LC3 and mitochondria in fibroblasts transduced with mitoDsRed and GFP-LC3 and treated with FCCP (30 $\mu$M) for 5 h ($N >= 17$) and (c) representative images (scale bar = 20 $\mu$m). (e) Size of LC3-puncta in fibroblasts treated with FCCP (30 $\mu$M) for 5 h. Results were normalized to the total number of LC3-puncta. Area is represented in $\mu m^2$ (XX axis) ($N >= 20$). Bar plots represent mean ± S.E.M and violin plots represent median with interquartile range. Statistical analysis: one-way ANOVA followed by Bonferroni multiple comparisons test: $^{*}p < 0.05$, $^{**}p < 0.01$, $^{***}p < 0.001$ or Kruskal-Wallis comparisons: $^{\phi\phi}p < 0.01$, $^{\phi\phi\phi}p < 0.001$, $^{\phi\phi\phi\phi}p < 0.0001$

fHD fibroblasts lines (Figure 2a). Only the cytosolic isoform of LC3 (LC3-I) was detected at basal levels in fCTRs and fpHD. The lipidated form of LC3-I (LC3-II) is recruited to autophagosomal membranes and rapidly degraded in active lysosomes which is consistent with functional autophagy machinery in fCTRs and fpHD (Figure 2a).

Additionally, we evaluated the autophagic flux in one fibroblast line from each group treated with CQ, which blocks protein degradation by lysosomal acidification, combined with FCCP to induce mitochondrial depolarization and fragmentation which precedes mitophagy. As expected, incubation with CQ/FCCP resulted in the accumulation of LC3-II, an increase of LC3-II/LC3-I ratio and accumulated p62 protein particularly in HD cell lines (Figure 2b). PINK1 protein levels increased only in cells from manifest HD patients. Protein LAMP2 is essential in controlling autolysosome formation and degradation of autophagosomes (Abokyi et al., 2021). The levels of LAMP2 decreased in manifest HD and control cells after treatment with the autophagy inhibitor CQ indicating downregulation of the lysosomal membrane-stabilizing and loss of lysosomal membrane integrity and function at a greater level than in pHD (Figure 2b).

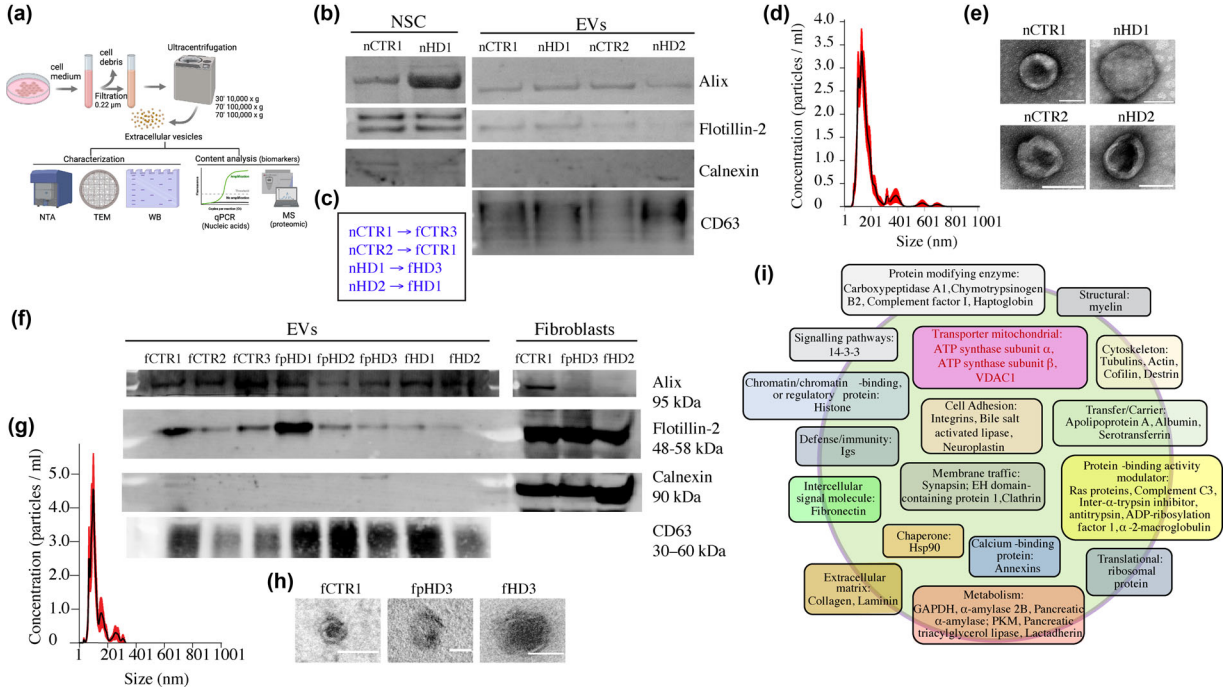


**FIGURE 3** Characterization of EVs isolated from fibroblasts and NSC of HD patients and controls. (a) Schematics of the ultracentrifugation protocol to obtain EVs and further application. (b, f) Western blot of NSC- and fibroblasts-EVs protein markers (Alix, Flotillin-2 and CD63) and Calnexin as a negative control. (c) Correspondence between differentiated NSC lines and patients' fibroblasts. (d, g) Representative analysis of NSC- and fibroblasts-EVs concentration (particles/ml) and size (nm) obtained by NTA, respectively. (e, h) TEM images of NSC- and fibroblasts-EVs, respectively (scale bar = 100 nm). (i) Mitochondrial associated proteins identified by mass spectrometry in NSC-EVs.

Together, these data showed an accumulation of proteins involved in detecting, targeting and eliminating dysfunctional mitochondria, suggesting impaired autophagosome-lysosome fusion or inhibition of lysosome degradative process in manifest HD.

We further investigated alterations in mitophagy through colocalization analysis in fibroblasts expressing a lysosomal fluorescence tagged protein (LC3-GFP) and a mitochondrial fluorescence tagged protein (mitoDsRed). We sought to evaluate the number, size, and colocalization of GFP-LC3 puncta with mitochondria under basal conditions and in the presence of FCCP to induce mitophagy or CQ to inhibit lysosomal degradation. The colocalization analysis of LC3 puncta with mitochondria showed no differences between treated and non-treated cell lines with FCCP, except for the one manifest HD cell line (fHD2) that showed an enhanced accumulation of LC3 puncta in mitochondria (Figures 2c, d). Interestingly, the fHD2 line also showed more p62 and PINK1 proteins upon exposure to auto/mitophagy modulators. Impairment of lysosomal degradation resulted in an augmented area of LC3-positive structures (Figure S3a). The puncta area was distributed by categories assuming that normal puncta had under 0.5 $\mu m^2$ and enlarged puncta had more than 0.5 $\mu m^2$. The increase in the area of LC3 puncta is cell-specific, as we observed an enlargement of puncta in fCTR2, fpHD3 and in one manifest HD cell line after acute mitophagy induction with FCCP (Figure 2e), suggesting increased enlarged autophagosomes in HD-fibroblasts upon promotion of mitochondrial elimination. No changes or slight reduction in size was observed in fCTR3, fpHD1 and fpHD2 (Figure 2e). The number of LC3 puncta was not altered, nor was the total number of puncta per cell area. Supplementary data show the histograms with the distribution of puncta in each area interval for every fibroblast line treated either with FCCP or CQ (Figure S3b, c). These data demonstrate that mitochondria seem to be more targeted for mitophagy in manifest HD cell lines.

## 3.3 | Fibroblasts and NSC from HD patients release more extracellular vesicles

To evaluate the release of small EVs by HD-fibroblasts, HD-NSC and CTRs lines we performed sequential ultracentrifugation to isolate these vesicles from conditioned growth media (Figure 3a, c). Characterization of EVs population according to ISEV guidelines (Théry et al., 2018) included the presence of typical protein markers for EVs such as Alix, Flotillin-2 and CD63; calnexin was used as a negative control to exclude cellular contaminants (Figure 3b, f). The NTA for particle size showed that EVs from fibroblasts and NSC were in the expected diameter ranging from 50 to 200 nm (Figure 3d, g). In addition, the EVs released by these cells exhibited the typical cap-shaped morphology (Figure 3e, h). To further assess the EVs proteomic cargo, isolated

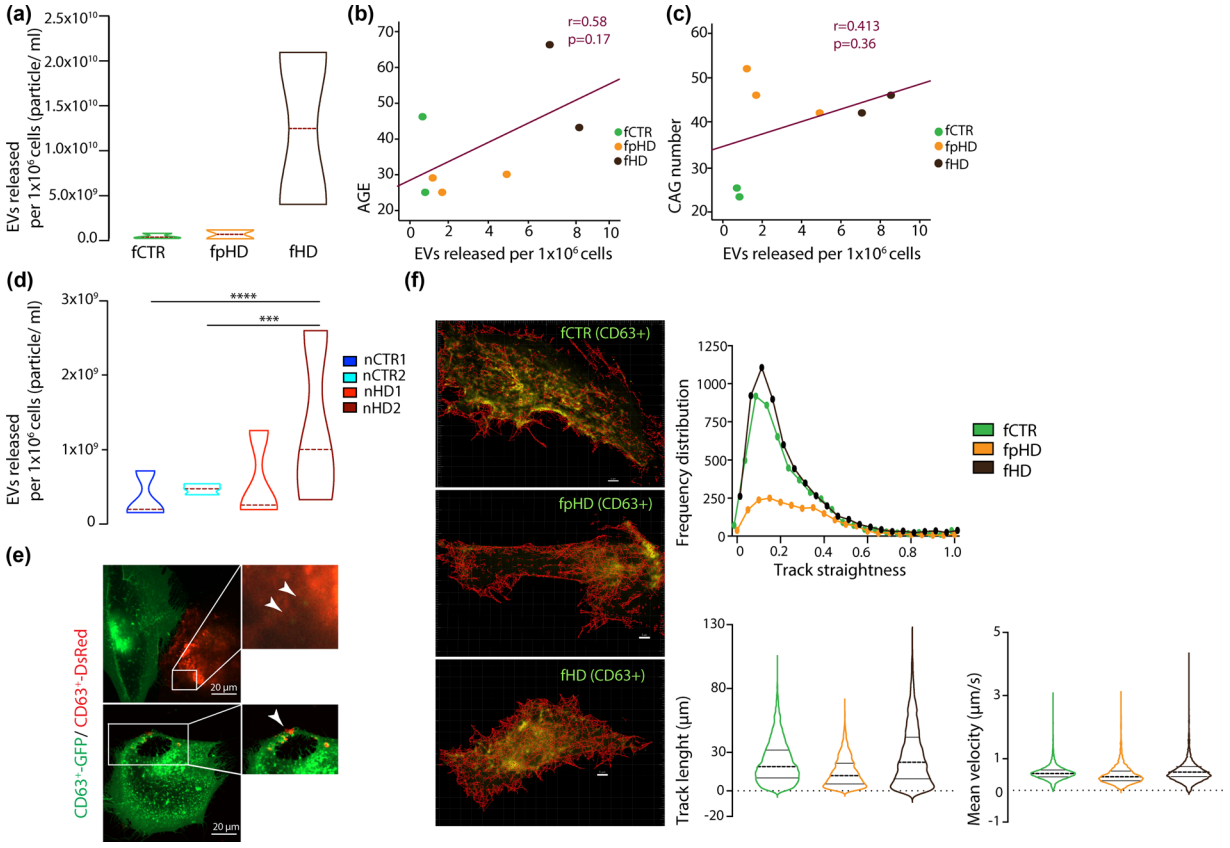


**FIGURE 4** Release of EVs is increased in HD cells. (a) Concentration of EVs released per 1x10^6 fibroblasts calculated by NTA (two control, three premanifest and two manifest HD fibroblasts were grouped). Correlation between EVs released per 1x10^6 fibroblasts and patients by (b) age and (c) CAG number. (d) Concentration of EVs released per 1x10^6 NSC calculated by NTA. (e) EVs exchange and uptake between a control line of fibroblasts transduced with CD63-GFP or CD63-DsRed (scale bar = 20 $\mu$m). (f) Single particle tracking (red traces in images) of EVs dynamics by confocal live cell imaging of CD63-GFP plasma membrane labelled fibroblasts (scale = 5 $\mu$m) and corresponding graphics of track straightness, track length ($\mu$m) and mean velocity ($\mu$m/s). Violin plots represent median with interquartile range. Statistical analysis: one-way ANOVA followed by Bonferroni multiple comparisons test: $^{***}p < 0.001$, $^{****}p < 0.0001$

EVs from HD- and CTR-NSC were analysed by liquid chromatography-tandem mass spectrometry (LC-MS/MS) (Figure 3i, S4). A combined analysis of the replicates identified 82 common proteins between HD-NSC and CTRs. These cell type-specific proteins were further submitted for gene enrichment analysis including Gene Ontology Biological Processes (Figure 3i). The analysis revealed an enrichment of proteins related to vesicles biogenesis, some cytoplasmic proteins and also proteins from intracellular organelles (e.g., mitochondria, lysosomes, endosomes) (Table S1). In fact, it was possible to detect the presence of some mitochondrial proteins, namely, VDAC-1, ATP synthase F1 subunit beta and subunit alpha within EVs. Heatmap analysis based on the relative abundance revealed that significantly different expressed proteins in NSC EVs are involved in metabolism, cell adhesion and membrane traffic (Figure S4a). The most enriched molecular functions included protein binding, structural molecule activity or catalytic and GTPase activity. In addition, protein–protein interaction network analysis (STRING database) showed that mitochondrial proteins, including ATP synthase subunits in the EVs were interrelated to each other (Figure S4b, c).

The rate of EVs secretion is a cell-specific process dependent on the physiological state or exposure to stimuli (Fader et al., 2008; Ma et al., 2018; Miranda et al., 2018). To study the effect of disease progression on EVs biodistribution, we next examined if the HD cells secreted more EVs. To test this, we evaluated the number of EVs secreted in conditioned media and observed that HD-fibroblasts and HD-NSC released more EVs compared to CTRs (Figure 4a, d). Next, we assessed if increased release could be affected by disease-specific parameters. Fibroblasts from older participants and with longer CAG repeats seemed to release a higher number of EVs suggesting that EVs secretion was increased with disease progression (Figure 4b, c). Importantly, control fibroblasts transduced with CD63-GFP or CD63-DsRed, when co-cultured for 24 h in low density, exchanged single vesicles, as shown in the visualization of green or red puncta in cells with a different CD63 tag (Figure 4e).

The single-particle tracking analysis of CD63+ EVs dynamics (Supplementary videos) shows that trajectories and speed in fpHD and fHD have a similar profile as fCTRs (Figure 4f). When evaluating the track straightness of EVs, all cell lines were more prone to random diffusion. Curiously, fpHD presented a decreased frequency distribution.

### 3.4 | HD-extracellular vesicles transport higher levels of mitochondrial genetic material

Mitochondrial DNA copy number is a biomarker of mitochondrial function (Castellani et al., 2020). Since our data shows decreased mitochondrial oxygen consumption rates and altered mitochondrial dynamics in fibroblasts and NSC of HD patients, we investigated the presence of mitochondrial genome and proteins in EVs. Using multiple approaches including long-range PCR, to screen the complete mitochondrial genome, and absolute DNA copy number, we detected mtDNA inside DNAse I-treated EVs (Figure 5a, b, c). Fibroblasts of CTRs and HD manifest patients had similar mtDNA copy numbers, but the EVs isolated from fHD1 showed increased number of mtDNA copies (Figure 5d). Premanifest carrier cells showed increased mtDNA copy number that was not translated into a corresponding higher EVs mtDNA content (Figure 5e). HD-EVs tend to transport a higher number of mtDNA copies compared to CTRs- and premanifest-EVs. mtDNA copy number in EVs was directly correlated with CAG expansion and number of EVs secreted (Figure 5f). Overall, these data indicate that mtDNA found inside EVs can be a biomarker for disease severity and possibly the generation of mitochondrial-derived vesicles (MDVs) could be a mechanism to counteract defective mitochondrial quality control (MQC). Surprisingly, the same results were not observed in NSC. EVs released from nHD2 line showed a tendency to have a higher number of mtDNA copies when compared to control cells. Still, EVs from nHD1 exhibited a very low number of mtDNA copies (Figure 5g).

Several lines of evidence suggest that there is a close interrelationship between autophagy and the regulation of EVs biogenesis and release by the cells (reviewed in Xu et al., 2018). Given our observation that cells from HD manifest patients show an increase in EVs release, we hypothesized that this is a consequence of autophagy impairment and mitochondrial dysfunction in the late stages of HD. To test this, EVs were isolated from control fibroblasts treated with FCCP for 5 h, with three times the concentration of the FCCP incubation for 16 h, or FCCP plus CQ for 16 h to induce mitochondrial fragmentation and inhibit the last stage of autophagy, respectively. Treated cells released more EVs than non-treated cells with higher number of mtDNA copies (Figure 5h, i). FCCP alone induces only a discrete increase suggesting that mitochondria-lysosomal axis deregulation is important for the increased shuttle of mtDNA in EVs. Treatment of these cells with GW4869, an inhibitor of EVs release, for 24 h, was used as a negative control. Therefore, the results support our hypothesis that alterations in autophagy efficiency and accumulation of damaged mitochondria in HD cells can induce the release of EVs with higher content in mtDNA and mitochondrial proteins.

Since a crosstalk between mitochondria and the EVs biogenesis pathways has been suggested (Su Chul Jang et al., 2019), next we performed live-cell microscopy analysis of fibroblasts expressing CD63-GFP or mitoDsRed. After co-culturing both cell populations, we observed the exchange of single vesicles (marked in green) and mitochondria (marked in red), as green or red puncta were visualized in cells with a different tag (Figure 6a). Moreover, we observed that EVs were able to travel along the lamellipodia towards the nucleus (not shown) and colocalize with mitochondria (Figure 6b). We further assessed the presence of other mitochondrial proteins within EVs through immunogold-TEM analysis and identified the presence of TFAM, a mitochondrial transcription factor (Figure 6c).

### 3.5 | Neuronal-derived EVs from human plasma carry mitochondrial DNA

To validate the potential of mtDNA as a biomarker for HD, total EVs and NDE were isolated from plasma of HD carriers and CTRs. NDE are a more specific subpopulation of EVs released by neuronal cells which reflects more accurately the biological mechanisms in neurons than the total pool of EVs present in human plasma. Western blotting analysis confirmed the presence of CD63 in both total EVs and NDE fractions. Moreover, L1CAM (protein of molecular adhesion in neurons) and synaptophysin (marker of presynaptic vesicles) were also detected as neuronal markers in NDE (Figure 7a). Characterization of total EVs and NDE by NTA confirmed the expected size for these vesicles (< 200 nm) (Figure 7b). NDE concentration isolated from total human plasma EVs was approximately 5%, as previously described (Sun et al., 2017) (Figure 7c). It was possible to detect the presence of the mitochondrially encoded 16S rRNA gene in the NDE population (Figure 7d). Interestingly, we found that mtDNA copy number was reduced in premanifest patients (30 and 40 copies) compared to prodromal and manifest patients (135 and 157 copies) (Figure 7d), suggesting that the number of mtDNA copies could be a neuronal indicator for the disease severity. These data would need to be confirmed in a larger sample size of HD patients and age-matched CTRs to validate their clinical relevance.

## 4 | DISCUSSION

Disruption of mitochondrial function and autophagy mechanisms are well-known features of HD (e.g., Lopes et al., 2022; Lopes et al., 2020; Rui et al., 2015). Indeed, there is an intricate crosstalk between mitochondrial dysfunction and cellular degradation pathways in neurodegenerative disorders.

Here, we demonstrate that NSC differentiated from HD patient's derived iPSC exhibited features of mitochondrial and metabolic impairment associated with lower levels of PGC-1α/TFAM, important regulators of mitochondrial biogenesis. We

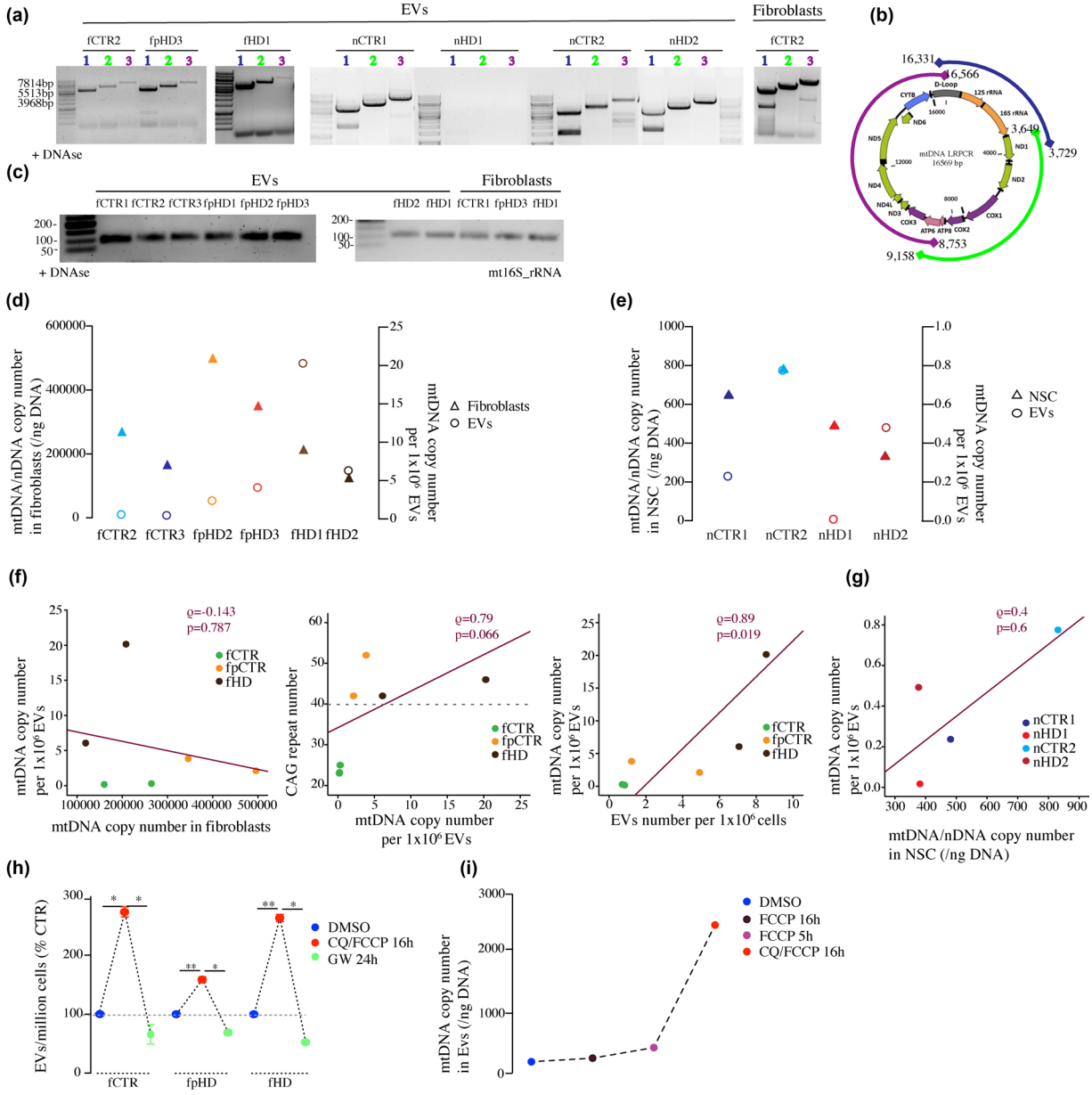


**FIGURE 5** Mitochondrial genome identified in EVs from HD and control cells. (a) Gel electrophoresis images of long-range PCR for mtDNA from purified EVs of fibroblasts (fCTR2-control, fpHD3- premanifest, fHD1- manifest HD lines) and NSC Fibroblast cell line used as controls. (b) schematic of primers for long-range PCR encoding the 16 kbp-size human mitochondrial genome. (c) Representative PCR gel electrophoresis of mtDNA (mt16S) of purified EVs of fibroblasts and NSC. EVs were pre-treated with 10 $\mu$g/$\mu$l of DNAse I. Fibroblasts cell line used as controls. (d) Absolute mtDNA copy number from fibroblasts and (e) NSC, and corresponding purified EVs. (f) Correlation between mtDNA copy number per 1x10^6 EVs and mtDNA copy number in corresponding cells, CAG number and number of released EVs per 1x10^6 cells, from left to right. (g) Correlation between absolute mtDNA copy number per 1x10^6 EVs and mtDNA/nuclear DNA copy number in NSC, normalized to ng of DNA. (h) Released EVs per 1x10^6 cells treated with chloroquine (CQ) (60 $\mu$M) and FCCP (10 $\mu$M) for 16 h to block lysosomal acidification and promote mitophagy, and GW4869 (30 $\mu$M) for 24 h to inhibit the EVs release. DMSO was used as control. (i) mtDNA copy number in EVs isolated from control fibroblasts treated with FCCP (10 $\mu$M) for 16 h, FCCP (30 $\mu$M) for 5 h, and CQ/FCCP (60 $\mu$M, 10 $\mu$M, respectively) for 16 h, normalized to ng of DNA. DMSO was used in control cells. Statistical analysis: one-way ANOVA followed by Bonferroni multiple comparisons test: $^*p < 0.5$, $^{**}p < 0.01$

documented in fibroblasts from the same donors, corresponding to patients with manifest HD, a general decrease in mitochondrial bioenergetic profile, increased levels of mitochondrial ROS production, and fragmentation associated with reduced mtDNA copy number compared with premanifest HD carriers (Lopes et al., 2022). Because defective mitochondria are eliminated by autophagy/mitophagy, we further explored in this study the impairment in autophagosomal pathway in these fibroblasts. We found that the levels of autophagy/mitophagy protein markers are increased in cells from manifest HD, suggesting an impaired autophagic degradation and/or increased autophagic induction. Of note, the accumulation of LAMP2, p62 and LC3-II in HD cells supports the hypothesis of impaired autophagosome/lysosome fusion since p62 is degraded via autophagy and the protein

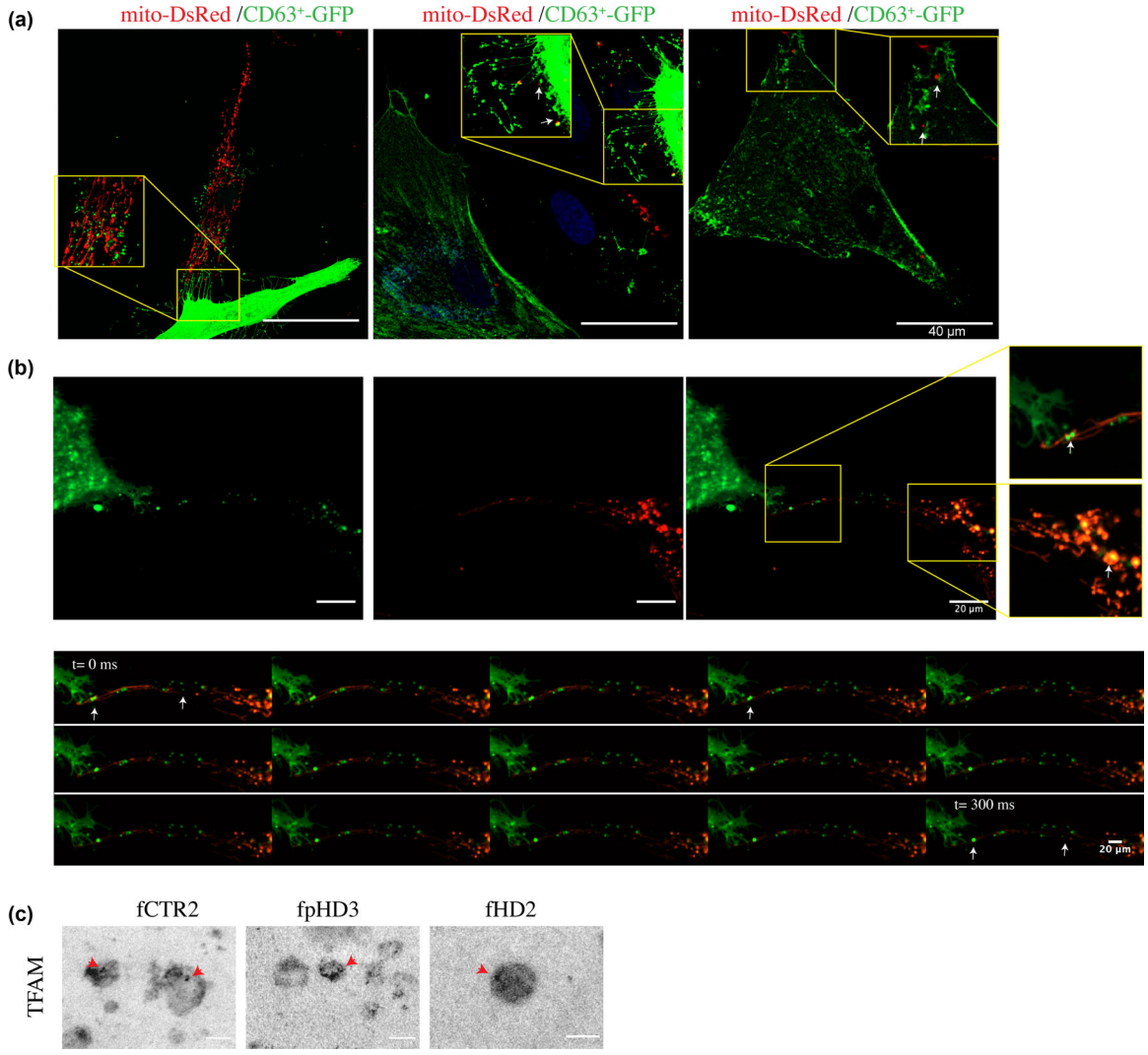


**FIGURE 6** EVs colocalize with mitochondria in fibroblasts. (a) EVs and mitochondria are interchanged between fibroblasts transduced with mito-DsRed or CD63-GFP (scale bar = 40 $\mu$m). (b) (Upper panel) Colocalization of mitochondria and CD63+- EVs shown by yellow puncta (arrow) (scale bar = 20 $\mu$m). (Lower panel) Time-lapse for 300 ms of EVs release (arrow) and mitochondrial dynamics in fibroblasts transduced with CD63-GFP and mito-DsRed, respectively (scale bar = 20 $\mu$m). (c) TFAM Immunogold staining in fibroblasts-EVs (fCTR2-control, fpHD3- premanifest, fHD2- manifest HD lines) (scale bar = 100 nm)

levels are inversely related to autophagic activity, LC3-II is proportional to the number of autophagosomes and LAMP2 protein is related to the levels of lysosomes (Yoshii & Mizushima, 2017). As observed previously, disruption in mitochondrial function can inhibit lysosomal activity and trigger the accumulation of large vacuoles positive for lysosomal markers in a mechanism mediated by ROS (Demers-Lamarche et al., 2016). Mitochondria are highly dynamic organelles dependent on efficient MQC to ensure correct mitochondrial plasticity, disposal, and replenishment mandatory for cellular homeostasis. Several pathways are involved in MQC, including mitophagy and MDVs generation. Mitophagy is a multi-step process where the dysfunctional organelle is initially engulfed into an autophagosome, which later fuses and delivers the cargo to lysosomes for degradation. Recently mitochondrial-lysosomal membrane contact sites were suggested to modulate mitochondrial dynamics either through intracellular calcium regulation or by regulating mitochondrial fission (Peng et al., 2020; Wong et al., 2018). Another line of defence involved in the elimination of damaged, oxidized mitochondria independent of mitochondrial depolarization, autophagy signalling, or mitochondrial fission are MDVs (Cadete et al., 2016; Neuspiel et al., 2008). Initially, it was proposed that the generation and upload of MDVs was regulated through a mechanism dependent on PINK1 and Parkin (McLelland et al., 2014). Recently, a new MDVs biogenesis pathway dependent on MIROs and DRP1 was described. Moreover, MDVs transport not only single proteins, but can also transport fully assembled complexes to lysosomes (König et al., 2021). The MDVs cargo can have two fates, the incorporation into the endolysosomal system through the fusion with multivesicular bodies, followed by lysosomal degradation or the secretion as EVs, or can be delivered into peroxisomes (D'Acunzo et al., 2021; Matheoud et al., 2016; Neuspiel et al., 2008; Soubannier et al., 2012). Several subtypes of MDVs have been identified based on their cargo selectivity and destination.

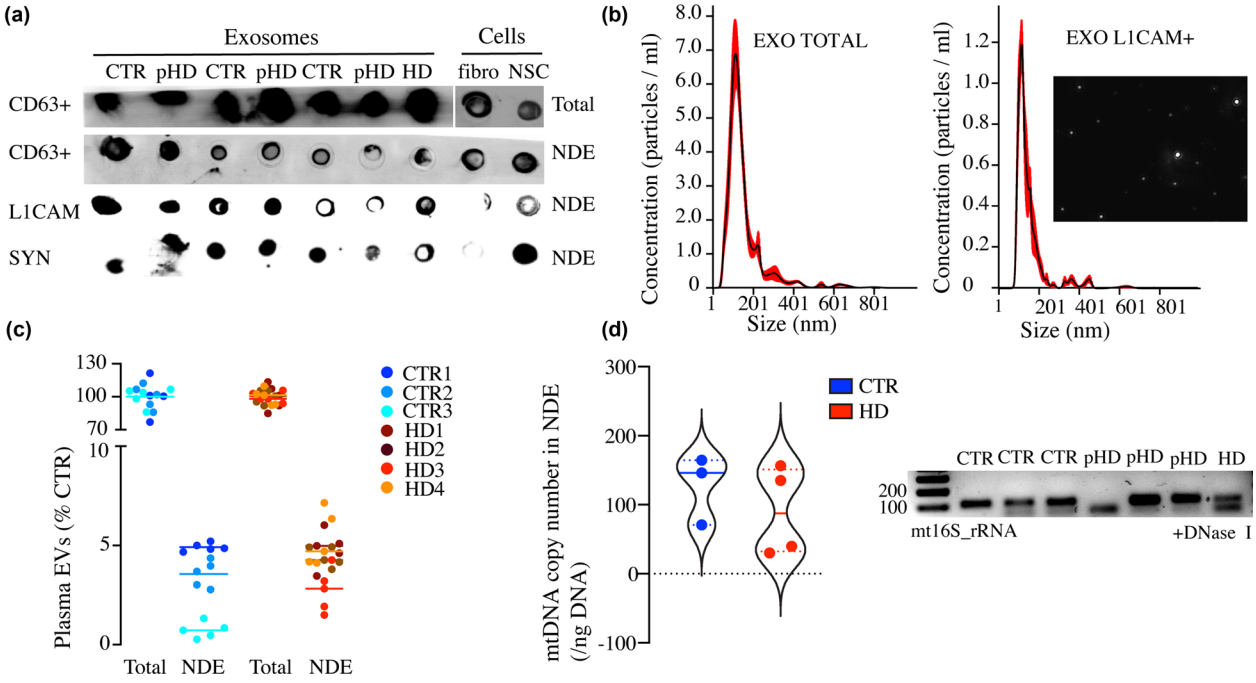


**FIGURE 7** Identification and quantification of neuronal derived exosomes (NDE). (a) Western blot showing NDE protein markers CD63, L1CAM and synaptophysin. (b) Concentration and diameter of plasma exosomes and NDE analysed by NTA. (c) Percentage of NDE extracted from whole plasma total EVs of HD patients and controls. (D) mtDNA absolute copy number detected in NDE and representative PCR gel electrophoresis. Free DNA was eliminated by DNase I digestion before isolation. Scatter dot plots represent mean ± SEM and violin plots median with interquartile range

These include the mitochondria-anchored protein ligase – containing MDVs, the pyruvate dehydrogenase (PDH)+/TOM20 - which traffic oxidized molecules into lysosomes and TOM20+/PDH- MDVs that also target the lysosomes but is a PINK1/Parkin independent pathway (McLelland et al., 2014; Soubannier et al., 2012).

Mitovesicles are another subclass of MDVs of endosomal origin that are secreted as EVs but are enriched in mitochondrial proteins such as VDAC, COX-IV and PDH-E1α (D'Acunzo et al., 2021). The proteomic analysis surprisingly revealed the presence of almost all electron transport chain and the PDH complex subunits (D'Acunzo et al., 2021). In this sense, lysosomal dysfunction and associated impaired autophagy can promote the release of MDVs through the endosomal pathway. Our data shows that manifest HD cells display mitochondrial dysfunction, increased mitophagy and impaired lysosome-mediated autophagy associated with an increased release of EVs and higher number of mtDNA copies. Interestingly, when we reproduced these conditions in control cells by inducing mitophagy and inhibiting autophagy the mtDNA content on EVs increased dramatically. Moreover, mutant HTT sequestration of autophagy proteins could exacerbate the disease progression by an age-dependent manner and thus EVs secretion could act as a compensatory mechanism to eliminate cellular stressors (Lee et al., 2012). Adipocyte cells also responded to mitochondrial stress and inhibition of lysosomal degradation by rapidly and robustly releasing EVs that contained oxidized mitochondria (Crewe et al., 2021). Interestingly, when these EVs are accumulated by cardiomyocytes, they can induce a transient mitochondrial oxidative stress, resulting in a protective compensatory antioxidant signalling (Crewe et al., 2021). In addition, as previously shown by other reports in breast cancer cells, fibroblast-derived EVs colocalize with mitochondria indicating that EVs can possibly fuse with targeted mitochondria in cells (Sansone et al., 2017). Our proteomic analysis of the EVs content validated previously established mitochondrial protein content (S. C. Jang et al., 2019; Peruzzotti-Jametti et al., 2021; Sansone et al., 2017). In general, the proportion of mitochondrial proteins described to be secreted within EVs is up to 10% of the total proteome (Sugiura et al., 2014). Increased EVs-associated secretion of mitochondrial proteins and DNA to compensate for the lysosomal impaired degradation add a new mechanism to the paradigms of MQC. Mito/autophagy are the classical pathways involved in removing of dysfunctional mitochondria, but when this degradative process is compromised, MDVs formation most likely complements this process by shuttling damaged, oxidized cargo through the endosome/exosome secretory pathway. Furthermore, recent evidence suggests that EVs can transfer between NSC structurally and functionally intact mitochondria with the ability to recover mitochondrial function in mtDNA-depleted cells paving new ways to the development of treatment strategies in neurodegenerative disorders (Peruzzotti-Jametti et al., 2021). In addition, we detected EVs-associated mtDNA in plasma-derived NDE from HD patients reinforcing the hypothesis of using NDE mtDNA as a possible biomarker for monitoring disease progression. Previous studies that addressed the NDE cargo focused mainly on microRNA or proteins of interest for the studied disease and only a few have focused on mitochondrial proteins (Goetzl et al., 2021). EVs derived from neurons are a new and controversial field that holds great potential as a liquid biopsy for the diagnostics of CNS diseases. Isolating brain

derived -EVs in biological fluids, such as cerebrospinal fluid (CSF) or blood, urine and saliva is a burgeoning field. The CSF-EVs hold great potential for biomarker discovery due to its proximity to the CNS (Thakur et al., 2021; Welton et al., 2017). However, the amount of EVs isolated in the CSF and the volume of CSF extracted from patients is more limited compared to peripheral fluids.

The role of MDVs as an MQC-associated mechanism or even its implication on the neuropathological processes underlying neurodegenerative disorders is unclear. mtDNA is commonly found in EVs secreted from different cells, yet the biological function is largely unknown (Elzanowska et al., 2021). Additionally, a decline in mtDNA levels with age in EVs from human plasma was reported (Lazo et al., 2021), supporting that our hypothesis of increased mtDNA levels in NDE from HD older patients is disease-dependent and not related to aging.

The mitochondrial content found in EVs, particularly mtDNA, is increasingly recognized as an agonist of the innate immune system capable of inducing an inflammatory response through various pattern-recognition receptors, including Toll-like receptors, NOD-like receptors and interferon-stimulatory DNA receptors (West & Shadel, 2017). Of relevance, pro-inflammatory mitochondrial proteins loading into EVs capable of inducing an immune response by triggering microglia to release pro-inflammatory factors to the extracellular media and consequently promote cell death have been reported in neurodegenerative diseases (Picca et al., 2019; Todkar et al., 2021; Wang et al., 2020). Limitations of the present work, which ought to be addressed in future studies, include: (1) The number of participants and the disease stage representativity; indeed, a comprehensive study enrolling an increased number of HD carriers and age-matched CTRs is necessary to better understand the impact of these results in disease pathophysiology; and (2) The results should be further confirmed in EVs released from patient's and control's iPSC-derived neurons.

Despite intensive investigation on the role of EVs, there are still several questions that remain to be answered, namely: Are EVs a mechanism to encapsulate and transfer mitochondrial material, genetic or proteic, to recipient cells, aiming to rescue their mitochondrial function, or is EVs-mediated secretion an alternative/compensatory mechanism, once autophagy is impaired, to eliminate defective mitochondria?

In conclusion, our data provide evidence of an innovative mechanism involving a dysfunction of the mitochondria-lysosomal axis that promotes the release of mitochondrial DNA and proteins within EVs. The MQC process comprises several pathways and, significantly in HD, MDVs trafficking seems to be part of a degradative mechanism complementary to mitophagy.

## AUTHOR CONTRIBUTIONS

Carla Lopes and A. Cristina Rego designed this study, Margarida Beatriz, Rita Vilaça, Carla Lopes, Sandra I. Anjo performed the experiments, Margarida Beatriz, Rita Vilaça, Carla Lopes analysed the data, Margarida Beatriz, Carla Lopes drafted the initial manuscript, Margarida Beatriz, Rita Vilaça, Carla Lopes, A. Cristina Rego revised this manuscript; all authors read and approved the final manuscript.

### ACKNOWLEDGEMENTS

We acknowledge Dr. Sandra Mota and Dr. Paulo Oliveira for their critical review of the manuscript, Dr. Mónica Zuzarte for fibroblasts and NSC TEM analysis at the 'Laboratório de Bio-imagem de Alta Resolução' of the Faculty of Medicine of the University of Coimbra, Dr. Teresa Rodrigues and Dr. Henrique Girão from Institute of Biomedical Imaging and Life Sciences (IBILI) of the Faculty of Medicine of the University of Coimbra for facilitating the access to NTA equipment Lab; Nurse Margarida from Neurology service of the 'Centro Hospitalar da Universidade de Coimbra' for the liaison with patients. This work was supported by the European Regional Development Fund (ERDF), through the Centro 2020 Regional Operational Programme under project CENTRO-01-0145-FEDER-000012-HealthyAging2020, and through the COMPETE2020–Operational Programme for Competitiveness and Internationalization and Portuguese national funds via FCT- Fundação para a Ciência e a Tecnologia, under project POCI-01-0145-FEDER-029621 and UIDB/04539/2020 and by Fundação Luso-Americana para o Desenvolvimento (FLAD) Life Science 2020 project.

### CONFLICT OF INTEREST

We declare no conflict of interest in this work.

### ORCID

*Carla Lopes* https://orcid.org/0000-0002-2543-8821

### REFERENCES

Abokyi, S., Shan, S.-W., Lam, C. H.-I., Catral, K. P., Pan, F., Chan, H. H.-L., To, C. - H., & Tse, D. Y.-Y. (2021). Targeting lysosomes to reverse hydroquinone-induced autophagy defects and oxidative damage in human retinal pigment epithelial cells. *International Journal of Molecular Sciences*, *22*(16), 9042.

Anjo, S. I., Santa, C., & Manadas, B. (2015). Short gelc-SWATH: A fast and reliable quantitative approach for proteomic screenings. *Proteomics*, *15*(4), 757–762.

Anjo, S. I., Simões, I., Castanheira, P., Grãos, M., & Manadas, B. (2019). Use of recombinant proteins as a simple and robust normalization method for untargeted proteomics screening: Exhaustive performance assessment. *Talanta*, *205*, 120163.

Beatriz, M., Vilaça, R., & Lopes, C. (2021). Exosomes: Innocent bystanders or critical culprits in neurodegenerative diseases. *Frontiers in Cell and Developmental Biology*, *9*, 1047.

Beckervordersandforth, R., Ebert, B., Schäffner, I., Moss, J., Fiebig, C., Shin, J., Moore, D. L., Ghosh, L., Trinchero, M. F., & Stockburger, C. (2017). Role of mitochondrial metabolism in the control of early lineage progression and aging phenotypes in adult hippocampal neurogenesis. *Neuron*, *93*(3), 560–573.

Beglinger, L. J., O'Rourke, J. J. F., Wang, C., Langbehn, D. R., Duff, K., Paulsen, J. S., & Huntington Study Group, I. (2010). Earliest functional declines in Huntington disease. *Psychiatry Research*, *178*(2), 414–418.

Cadete, V. J., Deschênes, S., Cuillerier, A., Brisebois, F., Sugiura, A., Vincent, A., Turnbull, D., Picard, M., McBride, H. M., & Burelle, Y. (2016). Formation of mitochondrial-derived vesicles is an active and physiologically relevant mitochondrial quality control process in the cardiac system. *Journal of Physiology*, *594*(18), 5343–5362.

Carmo, C., Naia, L., Lopes, C., & Rego, A. C. (2018). Mitochondrial dysfunction in huntington's disease. *Polyglutamine Disorders*, *1049*, 59–83.

Castellani, C. A., Longchamps, R. J., Sun, J., Guallar, E., & Arking, D. E. (2020). Thinking outside the nucleus: Mitochondrial DNA copy number in health and disease. *Mitochondrion*, *53*, 214–223.

Chambers, S. M., Fasano, C. A., Papapetrou, E. P., Tomishima, M., Sadelain, M., & Studer, L. (2009). Highly efficient neural conversion of human ES and iPS cells by dual inhibition of SMAD signaling. *Nature Biotechnology*, *27*(3), 275–280.

Coumans, F. A. W., Brisson, A. R., Buzas, E. I., Dignat-George, F., Drees, E. E. E., El-Andaloussi, S., Emanueli, C., Gasecka, A., Hendrix, A., Hill, A. F., Lacroix, R., Lee, Y., van Leeuwen, T. G., Mackman, N., Mäger, I., Nolan, J. P., van der Pol, E., Pegtel, D. M., Sahoo, S., … Nieuwland, R. (2017). Methodological guidelines to study extracellular vesicles. *Circulation Research*, *120*(10), 1632–1648.

Crewe, C., Funcke, J. B., Li, S., Joffin, N., Gliniak, C. M., Ghaben, A. L., An, Y. A., Sadek, H. A., Gordillo, R., Akgul, Y., Chen, S., Samovski, D., Fischer-Posovszky, P., Kusminski, C. M., Klein, S., & Scherer, P. E. (2021). Extracellular vesicle-based interorgan transport of mitochondria from energetically stressed adipocytes. *Cell Metabolism*, *33*(9), 1853–1868.e1811.

D'Acunzo, P., Pérez-González, R., Kim, Y., Hargash, T., Miller, C., Alldred, M. J., Erdjument-Bromage, H., Penikalapati, S. C., Pawlik, M., Saito, M., Ginsberg, S. D., Neubert, T. A., Goulbourne, C. N., & Levy, E. (2021). Mitovesicles are a novel population of extracellular vesicles of mitochondrial origin altered in down syndrome. *Science Advances*, *7*(7), eabe5085.

Dames, S., Eilbeck, K., & Mao, R. (2015). A high-throughput next-generation sequencing assay for the mitochondrial genome. *Mitochondrial Medicine*, Springer, 1264, 77–88.

Delli Carri, A., Onorati, M., Castiglioni, V., Faedo, A., Camnasio, S., Toselli, M., Biella, G., & Cattaneo, E. (2013). Human pluripotent stem cell differentiation into authentic striatal projection neurons. *Stem Cell Reviews and Reports*, *9*(4), 461–474.

Demers-Lamarche, J., Guillebaud, G., Tlili, M., Todkar, K., Bélanger, N., Grondin, M., Nguyen, A. P., Michel, J., & Germain, M. (2016). Loss of mitochondrial function impairs lysosomes. *Journal of Biological Chemistry*, *291*(19), 10263–10276.

Elzanowska, J., Semira, C., & Costa-Silva, B. (2021). DNA in extracellular vesicles: Biological and clinical aspects. *Molecular Oncology*, *15*(6), 1701–1714.

Evers, M. M., Schut, M. H., Pepers, B. A., Atalar, M., van Belzen, M. J., Faull, R. L. M., Roos, R. A. C., & van Roon-Mom, W. M. C. (2015). Making (anti-) sense out of huntingtin levels in huntington disease. *Molecular Neurodegeneration*, *10*(1), 1–11.

Fader, C. M., Sánchez, D., Furlán, M., & Colombo, M. I. (2008). Induction of autophagy promotes fusion of multivesicular bodies with autophagic vacuoles in k562 cells. *Traffic (Copenhagen, Denmark)*, *9*(2), 230–250.

Franco-Iborra, S., Plaza-Zabala, A., Montpeyo, M., Sebastian, D., Vila, M., & Martinez-Vicente, M. (2021). Mutant HTT (huntingtin) impairs mitophagy in a cellular model of Huntington disease. *Autophagy*, *17*(3), 672–689.

Gillet, L. C., Navarro, P., Tate, S., Röst, H., Selevsek, N., Reiter, L., Bonner, R., & Aebersold, R. (2012). Targeted data extraction of the MS/MS spectra generated by data-independent acquisition: A new concept for consistent and accurate proteome analysis. *Molecular & Cellular Proteomics*, *11*(6), O111.016717.

Goetzl, E. J., Wolkowitz, O. M., Srihari, V. H., Reus, V. I., Goetzl, L., Kapogiannis, D., Heninger, G. R., & Mellon, S. H. (2021). Abnormal levels of mitochondrial proteins in plasma neuronal extracellular vesicles in major depressive disorder. *Molecular Psychiatry*, *26*(12), 7355–7362.

Gonzalez-Hunt, C. P., Rooney, J. P., Ryde, I. T., Anbalagan, C., Joglekar, R., & Meyer, J. N. (2016). PCR-based analysis of mitochondrial DNA copy number, mitochondrial DNA damage, and nuclear DNA damage. *Current Protocols in Toxicology*, *67*(1), 20–11.

Jang, S. C., Crescitelli, R., Cvjetkovic, A., Belgrano, V., Olofsson Bagge, R., Sundfeldt, K., Ochiya, T., Kalluri, R., & Lötvall, J. (2019). Mitochondrial protein enriched extracellular vesicles discovered in human melanoma tissues can be detected in patient plasma. *Journal of Extracellular Vesicles*, *8*(1), 1635420.

Jia, L., Zhu, M., Kong, C., Pang, Y., Zhang, H., Qiu, Q., Wei, C., Tang, Y., Wang, Q., Li, Y., Li, T., Li, F., Wei, Y., & Jia, J. (2020). Blood neuro-exosomal synaptic proteins predict Alzheimer's disease at the asymptomatic stage. *Alzheimers Dement*, *17*(1), 49–60.

Johnson, S. M., Dempsey, C., Chadwick, A., Harrison, S., Liu, J., Di, Y., McGinn, O. J., Fiorillo, M., Sotgia, F., & Lisanti, M. P. (2016). Metabolic reprogramming of bone marrow stromal cells by leukemic extracellular vesicles in acute lymphoblastic leukemia. *Blood, The Journal of the American Society of Hematology*, *128*(3), 453–456.

Jędrak, P., Mozolewski, P., Węgrzyn, G., & Więckowski, M. R. (2018). Mitochondrial alterations accompanied by oxidative stress conditions in skin fibroblasts of huntington's disease patients. *Metabolic Brain Disease*, *33*(6), 2005–2017.

Katsu, M., Hama, Y., Utsumi, J., Takashina, K., Yasumatsu, H., Mori, F., Wakabayashi, K., Shoji, M., & Sasaki, H. (2019). MicroRNA expression profiles of neuron-derived extracellular vesicles in plasma from patients with amyotrophic lateral sclerosis. *Neuroscience Letters*, *708*, 134176.

König, T., Nolte, H., Aaltonen, M. J., Tatsuta, T., Krols, M., Stroh, T., Langer, T., & McBride, H. M. (2021). MIROs and DRP1 drive mitochondrial-derived vesicle biogenesis and promote quality control. *Nature Cell Biology*, *23*(12), 1271–1286.

Lazo, S., Noren Hooten, N., Green, J., Eitan, E., Mode, N. A., Liu, Q. R., Zonderman, A. B., Ezike, N., Mattson, M. P., Ghosh, P., & Evans, M. K. (2021). Mitochondrial DNA in extracellular vesicles declines with age. *Aging Cell*, *20*(1), E13283.

Lee, H., Noh, J. Y., Oh, Y., Kim, Y., Chang, J. W., Chung, C. W., Lee, S. T., Kim, M., Ryu, H., & Jung, Y. K. (2012). IRE1 plays an essential role in ER stress-mediated aggregation of mutant huntingtin via the inhibition of autophagy flux. *Human Molecular Genetics*, *21*(1), 101–114.

Leidal, A. M., Huang, H. H., Marsh, T., Solvik, T., Zhang, D., Ye, J., Kai, F., Goldsmith, J., Liu, J. Y., & Huang, Y. - H. (2020). The LC3-conjugation machinery specifies the loading of RNA-binding proteins into extracellular vesicles. *Nature Cell Biology*, *22*(2), 187–199.

Lemiere, J., Decruyenaere, M., Evers-Kiebooms, G., Vandenbussche, E., & Dom, R. (2004). Cognitive changes in patients with Huntington's disease (HD) and asymptomatic carriers of the HD mutation. *Journal of Neurology*, *251*(8), 935–942.

Lopes, C., Ferreira, I. L., Maranga, C., Beatriz, M., Mota, S. I., Sereno, J., Castelhano, J., Abrunhosa, A., Oliveira, F., De Rosa, M., Hayden, M., Laço, M. N., Januário, C., Branco, M. C., & Rego, A. C. (2022). Mitochondrial and redox modifications in early stages of Huntington's disease. *Redox biology*, *56*, 102424.

Lopes, C., Tang, Y., Anjo, S. I., Manadas, B., Onofre, I., De Almeida, L. P., Daley, G. Q., Schlaeger, T. M., & Rego, A. C. (2020). Mitochondrial and redox modifications in Huntington disease induced pluripotent stem cells rescued by CRISPR/Cas9 CAGs targeting. *Frontiers in Cell and Developmental Biology*, *8*, 576592.

Ma, C., Wang, J., Liu, H., Chen, Y., Ma, X., Chen, S., Bihl, J. I., & Yang, Y. I. (2018). Moderate exercise enhances endothelial progenitor cell exosomes release and function. *Medicine and Science in Sports and Exercise*, *50*(10), 2024–2032.

MacDonald, M. E., Ambrose, C. M., Duyao, M. P., Myers, R. H., Lin, C., Srinidhi, L., Barnes, G., Taylor, S. A., James, M., & Groot, N. (1993). A novel gene containing a trinucleotide repeat that is expanded and unstable on Huntington's disease chromosomes. *Cell*, *72*(6), 971–983.

Matheoud, D., Sugiura, A., Bellemare-Pelletier, A., Laplante, A., Rondeau, C., Chemali, M., Fazel, A., Bergeron, J. J., Trudeau, L. E., Burelle, Y., Gagnon, E., McBride, H. M., & Desjardins, M. (2016). Parkinson's disease-related proteins PINK1 and parkin repress mitochondrial antigen presentation. *Cell*, *166*(2), 314–327.

McLelland, G. L., Soubannier, V., Chen, C. X., McBride, H. M., & Fon, E. A. (2014). Parkin and PINK1 function in a vesicular trafficking pathway regulating mitochondrial quality control. *Embo Journal*, *33*(4), 282–295.

Mehrabi, N. F., Waldvogel, H. J., Tippett, L. J., Hogg, V. M., Synek, B. J., & Faull, R. L. M. (2016). Symptom heterogeneity in Huntington's disease correlates with neuronal degeneration in the cerebral cortex. *Neurobiology of Disease*, *96*, 67–74.

Merrill, R. A., Flippo, K. H., & Strack, S. (2017). Measuring mitochondrial shape with imageJ. ( pp. 31–48) *Techniques to investigate mitochondrial Function in neurons*, Springer.

Miranda, A. M., Lasiecka, Z. M., Xu, Y., Neufeld, J., Shahriar, S., Simoes, S., Chan, R. B., Oliveira, T. G., Small, S. A., & Di Paolo, G. (2018). Neuronal lysosomal dysfunction releases exosomes harboring APP C-terminal fragments and unique lipid signatures. *Nature Communications*, *9*(1), 1–16.

Neuspiel, M., Schauss, A. C., Braschi, E., Zunino, R., Rippstein, P., Rachubinski, R. A., Andrade-Navarro, M. A., & McBride, H. M. (2008). Cargo-selected transport from the mitochondria to peroxisomes is mediated by vesicular carriers. *Current Biology*, *18*(2), 102–108.

Nicoleau, C., Varela, C., Bonnefond, C., Maury, Y., Bugi, A., Aubry, L., Viegas, P., Bourgois-Rocha, F., Peschanski, M., & Perrier, A. L. (2013). Embryonic stem cells neural differentiation qualifies the role of Wnt/$\beta$-Catenin signals in human telencephalic specification and regionalization. *Stem Cells*, *31*(9), 1763–1774.

Niu, M., Li, Y., Li, G., Zhou, L., Luo, N., Yao, M., Kang, W., & Liu, J. (2020). A longitudinal study on $\alpha$-synuclein in plasma neuronal exosomes as a biomarker for Parkinson's disease development and progression. *European Journal of Neurology*, *27*(6), 967–974.

O'Brien, K., Breyne, K., Ughetto, S., Laurent, L. C., & Breakefield, X. O. (2020). RNA delivery by extracellular vesicles in mammalian cells and its applications. *Nature Reviews Molecular Cell Biology*, *21*(10), 585–606.

Peng, W., Wong, Y. C., & Krainc, D. (2020). Mitochondria-lysosome contacts regulate mitochondrial ca. *Proceedings of the National Academy of Sciences of the United States of America*, *117*(32), 19266–19275.

Peruzzotti-Jametti, L., Bernstock, J. D., Willis, C. M., Manferrari, G., Rogall, R., Fernandez-Vizarra, E., Williamson, J. C., Braga, A., van den Bosch, A., Leonardi, T., Krzak, G., Kittel, Á., Benincá, C., Vicario, N., Tan, S., Bastos, C., Bicci, I., Iraci, N., Smith, J. A., … Pluchino, S. (2021). Neural stem cells traffic functional mitochondria via extracellular vesicles. *Plos Biology*, *19*(4), E3001166.

Picca, A., Guerra, F., Calvani, R., Bucci, C., Lo Monaco, M. R., Bentivoglio, A. R., Landi, F., Bernabei, R., & Marzetti, E. (2019). Mitochondrial-Derived vesicles as candidate biomarkers in Parkinson's disease: Rationale, design and methods of the EXosomes in PArkiNson disease (EXPAND) study. *International Journal of Molecular Sciences*, *20*(10), 2373.

Pircs, K., Petri, R., Madsen, S., Brattås, P. L., Vuono, R., Ottosson, D. R., St-Amour, I., Hersbach, B. A., Matusiak-Brückner, M., & Lundh, S. H. (2018). Huntingtin aggregation impairs autophagy, leading to argonaute-2 accumulation and global microRNA dysregulation. *Cell Reports*, *24*(6), 1397–1406.

Rui, Y. N., Xu, Z., Patel, B., Chen, Z., Chen, D., Tito, A., David, G., Sun, Y., Stimming, E. F., Bellen, H. J., Cuervo, A. M., & Zhang, S. (2015). Huntingtin functions as a scaffold for selective macroautophagy. *Nature Cell Biology*, *17*(3), 262–275.

Sansone, P., Savini, C., Kurelac, I., Chang, Q., Amato, L. B., Strillacci, A., Stepanova, A., Iommarini, L., Mastroleo, C., Daly, L., Galkin, A., Thakur, B. K., Soplop, N., Uryu, K., Hoshino, A., Norton, L., Bonafé, M., Cricca, M., Gasparre, G., … Bromberg, J. (2017). Packaging and transfer of mitochondrial DNA via exosomes regulate escape from dormancy in hormonal therapy-resistant breast cancer. *Proceedings of the National Academy of Sciences of the United States of America*, *114*(43), E9066–E9075.

Schlaeger, T. M., Daheron, L., Brickler, T. R., Entwisle, S., Chan, K., Cianci, A., DeVine, A., Ettenger, A., Fitzgerald, K., & Godfrey, M. (2015). A comparison of non-integrating reprogramming methods. *Nature Biotechnology*, *33*(1), 58–63.

Sennels, L., Bukowski-Wills, J. - C., & Rappsilber, J. (2009). Improved results in proteomics by use of local and peptide-class specific false discovery rates. *BMC Bioinformatics [Electronic Resource]*, *10*(1), 1–11.

Shirendeb, U. P., Calkins, M. J., Manczak, M., Anekonda, V., Dufour, B., McBride, J. L., Mao, P., & Reddy, P. H. (2012). Mutant huntingtin's interaction with mitochondrial protein drp1 impairs mitochondrial biogenesis and causes defective axonal transport and synaptic degeneration in huntington's disease. *Human Molecular Genetics*, *21*(2), 406–420.

Soubannier, V., McLelland, G. L., Zunino, R., Braschi, E., Rippstein, P., Fon, E. A., & McBride, H. M. (2012). A vesicular transport pathway shuttles cargo from mitochondria to lysosomes. *Current Biology*, *22*(2), 135–141.

Sugiura, A., McLelland, G. L., Fon, E. A., & McBride, H. M. (2014). A new pathway for mitochondrial quality control: Mitochondrial-derived vesicles. *EMBO Journal*, *33*(19), 2142–2156.

Sun, B., Dalvi, P., Abadjian, L., Tang, N., & Pulliam, L. (2017). Blood neuron-derived exosomes as biomarkers of cognitive impairment in HIV. *AIDS (London, England)*, *31*(14), F9.

Tang, W. H., Shilov, I. V., & Seymour, S. L. (2008). Nonlinear fitting method for determining local false discovery rates from decoy database searches. *Journal of Proteome Research*, *7*(9), 3661–3667.

Thakur, A., Xu, C., Li, W. K., Qiu, G., He, B., Ng, S. P., Wu, C. L., & Lee, Y. (2021). In vivo liquid biopsy for glioblastoma malignancy by the AFM and LSPR based sensing of exosomal CD44 and CD133 in a mouse model. *Biosensors & Bioelectronics*, *191*, 113476.

Thompson, J. C., Harris, J., Sollom, A. C., Stopford, C. L., Howard, E., Snowden, J. S., & Craufurd, D. (2012). Longitudinal evaluation of neuropsychiatric symptoms in Huntington's disease. *The Journal of Neuropsychiatry and Clinical Neurosciences*, *24*(1), 53–60.

Théry, C., Amigorena, S., Raposo, G., & Clayton, A. (2006). Isolation and characterization of exosomes from cell culture supernatants and biological fluids. *Current Protocols in Cell Biology*, **Chapter 3**: Unit 30: 3.22.1-3.22.29.

Théry, C., Witwer, K. W., Aikawa, E., Alcaraz, M. J., Anderson, J. D., Andriantsitohaina, R., Antoniou, A., Arab, T., Archer, F., Atkin-Smith, G. K., Ayre, D. C., Bach, J. M., Bachurski, D., Baharvand, H., Balaj, L., Baldacchino, S., Bauer, N. N., Baxter, A. A., Bebawy, M., … Zuba-Surma, E. K. (2018). Minimal information for studies of extracellular vesicles 2018 (MISEV2018): A position statement of the international society for extracellular vesicles and update of the MISEV2014 guidelines. *Journal of Extracellular Vesicles*, *7*(1), 1535750.

Tiscornia, G., Singer, O., & Verma, I. M. (2006). Production and purification of lentiviral vectors. *Nature Protocols*, *1*(1), 241–245.

Todkar, K., Chikhi, L., Desjardins, V., El-Mortada, F., Pépin, G., & Germain, M. (2021). Selective packaging of mitochondrial proteins into extracellular vesicles prevents the release of mitochondrial DAMPs. *Nature Communication*, *12*(1), 1971.

Vonsattel, J. P. G., Keller, C., & del Pilar Amaya, M. (2008). Neuropathology of Huntington's disease. *Handbook of Clinical Neurology*, *89*, 599–618.

Wang, X., Weidling, I., Koppel, S., Menta, B., Ortiz, J. P., Kalani, A., Wilkins, H. M., & Swerdlow, R. H. (2020). Detection of mitochondria-pertinent components in exosomes. *Mitochondrion*, *55*, 100–110.

Welton, J. L., Loveless, S., Stone, T., von Ruhland, C., Robertson, N. P., & Clayton, A. (2017). Cerebrospinal fluid extracellular vesicle enrichment for protein biomarker discovery in neurological disease; multiple sclerosis. *Journal of Extracellular Vesicles*, *6*, 1369805.

West, A. P., & Shadel, G. S. (2017). Mitochondrial DNA in innate immune responses and inflammatory pathology. *Nature Reviews Immunology*, *17*(6), 363–375.

Winston, C. N., Romero, H. K., Ellisman, M., Nauss, S., Julovich, D. A., Conger, T., Hall, J. R., Campana, W., O'Bryant, S. E., & Nievergelt, C. M. (2019). Assessing neuronal and astrocyte derived exosomes from individuals with mild traumatic brain injury for markers of neurodegeneration and cytotoxic activity. *Frontiers in Neuroscience*, *13*, 1005.

Wong, Y. C., Ysselstein, D., & Krainc, D. (2018). Mitochondria-lysosome contacts regulate mitochondrial fission via RAB7 GTP hydrolysis. *Nature*, *554*(7692), 382–386.

Xu, J., Camfield, R., & Gorski, S. M. (2018). The interplay between exosomes and autophagy–partners in crime. *Journal of Cell Science*, *131*(15), Jcs215210.

Yoshii, S. R., & Mizushima, N. (2017). Monitoring and measuring autophagy. *International Journal of Molecular Sciences*, *18*(9), 1865.

Yousif, G., Qadri, S., Parray, A., Akhthar, N., Shuaib, A., & Haik, Y. (2021). Exosomes derived neuronal markers: Immunoaffinity isolation and characterization. *Neuromolecular Medicine*, *24*(3), 339–351.

Zala, D., Hinckelmann, M. - V., Yu, H., Da Cunha, M. M. L., Liot, G., Cordelières, F. P., Marco, S., & Saudou, F. (2013). Vesicular glycolysis provides on-board energy for fast axonal transport. *Cell*, *152*(3), 479–491.

## SUPPORTING INFORMATION

Additional supporting information can be found online in the Supporting Information section at the end of this article.

**How to cite this article:** Beatriz, M., Vilaça, R., Anjo, S. I., Manadas, B., Januário, C., Rego, A. C., & Lopes, C. (2022). Defective mitochondria-lysosomal axis enhances the release of extracellular vesicles containing mitochondrial DNA and proteins in huntington's disease. *Journal of Extracellular Biology*, *1,* e65. https://doi.org/10.1002/jex2.65